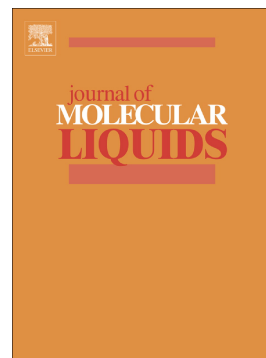


Effect of the active phase-support interaction on the electronic, thermal and catalytic properties of [H-Pyr]+[HSO₄]-/support (support=rice husk ash; corundum)



Ivaylo Tankov, Romyana Yankova, Anife Veli, Radoslava Nikolova, Zilya Mustafa, Ivanka Stoycheva

PII: S0167-7322(20)33441-3

DOI: <https://doi.org/10.1016/j.molliq.2020.113725>

Reference: MOLLIQ 113725

To appear in: *Journal of Molecular Liquids*

Received date: 29 May 2020

Revised date: 25 June 2020

Accepted date: 30 June 2020

Please cite this article as: I. Tankov, R. Yankova, A. Veli, et al., Effect of the active phase-support interaction on the electronic, thermal and catalytic properties of [H-Pyr]+[HSO₄]-/support (support=rice husk ash; corundum), *Journal of Molecular Liquids* (2020), <https://doi.org/10.1016/j.molliq.2020.113725>

This is a PDF file of an article that has undergone enhancements after acceptance, such as the addition of a cover page and metadata, and formatting for readability, but it is not yet the definitive version of record. This version will undergo additional copyediting, typesetting and review before it is published in its final form, but we are providing this version to give early visibility of the article. Please note that, during the production process, errors may be discovered which could affect the content, and all legal disclaimers that apply to the journal pertain.

Effect of the active phase-support interaction on the electronic, thermal and catalytic properties of [H-Pyr]⁺[HSO₄]⁻/Support (Support = rice husk ash; corundum)

*Ivaylo Tankov¹, Romyana Yankova¹, Anife Veli¹,
Radoslava Nikolova¹, Zilya Mustafa¹, Ivanka Stoycheva²*

¹University "Prof. Dr. Assen Zlatarov" Burgas, 8010, Bulgaria

²Institute of Organic Chemistry with Centre of Phytochemistry, Bulgarian Academy of Sciences, Bulgaria

Abstract

Influence of the surface active phase-support interaction on the electronic, thermal and catalytic performance of pyridinium hydrogen sulfate ([H-Pyr]⁺[HSO₄, PHS]⁻) ionic liquid immobilized by a wetness impregnation method on rice husk ash (RHA) and corundum (Al-NA) carriers has been investigated in the current work. For that purpose, both the developed supports and the corresponding catalysts (PHS/Al-NA and PHS/RHA) were characterized in details by means of analytical methods such as N₂ adsorption-desorption measurements, X-ray diffraction, X-ray photoelectron spectroscopy, spectroscopy in the ultraviolet and visible regions, infrared spectroscopy and thermogravimetric analysis. To compare the catalytic activity of PHS/Al-NA and PHS/RHA, a process of butyl acetate synthesis was applied as a test reaction. The physicochemical characterization revealed that the active phase-support interaction in the case of PHS/RHA catalyst is stronger than that between PHS phase and Al-NA. Based on this, the catalytic performance of PHS/RHA sample (expressed by substrate conversion degree) in the reaction of acetic acid esterification with butanol was found to be more pronounced with respect to that of Al-NA supported pyridinium hydrogen sulfate.

Keywords: Supported ionic liquids; Physicochemical characterization; Thermal behavior; Catalytic properties

1. Introduction

Over the past few decades, the ionic liquids (ILs) investigation is a major field in the modern chemistry due to their unique properties – low vapor pressure, high thermal stability, tunable polarity and high conductivity [1]. Ionic liquids are molten salts (melt at or below 100°C), consisting of organic cations associated with organic or inorganic anions [2]. The anion and cation variety allows changing of the ILs properties according to a specific application. Besides as a “green” alternative to volatile organic solvents, the ILs application as homogeneous catalysts for various organic reactions is widely reported [3,4]. Tao et al. [3] present acetic acid esterification with C₁–C₄ alcohols in the presence of the ionic liquid [C₁Im]⁺[HSO₄]⁻. In the field of organic synthesis, the alkylation of phenol with tert-butyl alcohol as an alkylating agent is studied in presence of [C₄C₁Im]⁺[X]⁻ (X = Cl, BF₄, PF₆) [5]. Maximum phenol conversion of 93% at molar ratio of phenol:TBA:IL of 1:2:1, reaction time of 3 h and reaction temperature of 80°C is achieved. However, the ILs application as homogeneous catalysts have several drawbacks: (i) usage of large amounts of ILs for high reactants conversion, (ii) mass transfer limitations due to high ILs viscosity, (iii) difficult IL catalyst separation from the reaction products [6]. To overcome the aforementioned disadvantages, the ILs immobilization on solid supports is extensively studied [7].

Immobilisation of ILs can be carried out by several methods: (i) solid supports impregnation with IL, (ii) creating covalent bonds between the IL and the support, (iii) a of IL confinement in the support material or (iv) copolymerisation of the IL with a suitable monomer. Covalent bonds may be formed between the IL and the support even when the SILP is obtained by impregnation – in case of chloroaluminate ILs where anions are attached through the metal centre of the anion to a surface OH group [8]. Non-covalent interactions of the functional groups of anions, such as the SO₃ group of [OTf]⁻, with solid surfaces were also detected by IR measurements [9].

The supported ionic liquid (SILs) catalysts combine the advantages of the ILs and those of the solid support. Compared with pure ILs, SILs offer further benefits such as easy separation, reusability and application in fixed or fluidized bed reactors. It should be further emphasized that even a very low solubility of the catalyst in the flowing liquid media will make long term stability of the SILC catalyst system impossible due to slow but steady leaching. Moreover, almost identical catalytic activity between the SILs and their

homogenous counterparts was shown as well [10]. Different materials have been used as solid supports for SILs preparation [11]. Brønsted acidic SILs can be prepared by the use of $[\text{HSO}_4]^-$ or $[\text{H}_2\text{PO}_4]^-$ anions or by the introduction of alkane sulfonic acid groups as side chains of the cations. Combination of these two approaches leads to the so called “dual acidic” ionic liquids. For example, Wang et al. [10] investigate the catalytic activity of $[\text{C}_4\text{SO}_3\text{HC}_1\text{Im}]^+[\text{X}]^-$ ($\text{X} = [\text{HSO}_4]^-$, $[\text{H}_2\text{PO}_4]^-$ and CF_3COO^-) supported on various solids (SiO_2 , Al_2O_3 , ZrO_2 , TiO_2) in esterification of pentaerythritol with caproic acid. The results showed that the $[\text{C}_4\text{SO}_3\text{HC}_1\text{Im}]^+[\text{HSO}_4]^-/\text{SiO}_2$ sample possesses the best catalytic activity, expressed by ester yield value of 99%. In another work, alkylation of benzene with 1-dodecene over SBA-15 supported $[\text{C}_4\text{C}_1\text{Im}]^+[\text{TFSI}]^-$ is investigated [11]. A promising alternative of the SiO_2 support for SILs catalysts could be rice husk ash [12], a major waste product of the rice milling industry. Usage of $[\text{C}_1(\text{CH}_3\text{O})_3\text{SiC}_3\text{Im}]^+[\text{HSO}_4]^-/\text{RHA}$ in 1-(benzothiazolylamino)-phenylmethyl-2-naphthols and pyrimido[1,2-a]benzimidazole synthesis showed product yields of 97 and 93%, respectively [13].

It is well known that the support nature significantly influences the catalytic behavior of a heterogeneous catalyst due to an active phase-support interaction [14]. Hence, to predict the properties of SILs catalysts and choose a more suitable one for a specific application, a detailed analysis on the IL-support interaction is needed. The degree of ILs immobilization on the solid support surface and the ILs-support interaction as well can be successfully studied using different analytical techniques such as specific surface area measurements, X-ray diffraction (XRD), X-ray photoelectron spectroscopy (XPS), spectroscopy in the ultraviolet and visible regions (UV-vis), Fourier transform infrared spectroscopy (FT-IR) and thermogravimetric analysis (TGA).

The aim of the present work is to study the effect of the surface active phase-support interaction on the catalytic properties of new SILs, namely pyridinium hydrogen sulfate immobilized on rice husk ash and corundum carriers. For that purpose, a combination of analytical techniques (N_2 adsorption-desorption measurement, XRD, XPS, UV-vis, FT-IR, TGA/DSC) is applied for a physicochemical characterization of the samples. To compare the catalytic activity of the obtained SILs, acetic acid esterification with 1-butanol is used as a test reaction. The results are expected to be useful for future experimental and theoretical studies on the structure-activity relationship in different types of supported ionic liquids.

2. Experimental section

2.1. Preparation of pyridinium hydrogen sulfate

Pyridine (2.13 g, 0.0269 mol) and ultra clean water (1.45 g, 0.0807 mol) were charged into a 0.020 l three-necked flat bottom reactor, equipped with a magnetic stirring, a reflux condenser and a thermometer. The aqueous solution of pyridine was stirred at ambient temperature for 0.5h, where after the temperature was reduced to 5°C. Then, H₂SO₄ (2.64 g, 0.0269 mol) was added dropwise over a period of 1.5 h under vigorous stirring. The reaction mixture was stirred at reflux for an additional period of 5 h at 80°C. For solvent removing, the aqueous solution of pyridinium hydrogen sulfate was distilled at 70°C under reduced pressure (0.050 MPa) and the product was dried at the same conditions for 8 h until the residue mass remained constant. After cooling, the colorless solid was washed three times with diethyl ether 0.100 l and dried under vacuum (0.050 MPa) at 80°C for 12 h. Pyridinium hydrogen sulfate is denoted as PHS.

2.2. Preparation of rice husk ash

Rice husk ash, abbreviated as RHA, is obtained by controlled rice husk combustion in air through a fluidized bed reactor lab-scale installation at a temperature of 320°C and a heating rate of 10°C/min.

2.3. Synthesis of corundum

Corundum synthesis includes a pre-formation of ammonium alum (NH₄Al(SO₄)₂·12H₂O) from ammonium and aluminum sulfates in water solution at 70°C. After cooling for 2 h, a white precipitate was formed. It was filtered and washed in deionized water several times. The powder produced was calcined at 1000°C for 1 h to obtain α-Al₂O₃ (denoted in the paper as Al-NA)

2.4 Preparation of supported pyridinium hydrogen sulfate

The supported ionic liquid is obtained by wetness impregnation of the synthesized supports (RHA and Al-NA) (3g) with an aqueous solution (0.0271 mol/l, 66 wt.% PHS with respect to the support mass) of PHS in a round bottom flask (0.100 l). The mixture is intensively stirred (1000 rpm) at ambient temperature for 30 h. The water is removed in a rota-

ry evaporator at 70°C and reduced pressure (0.010 MPa). The solids (PHS/RHA and PHS/Al-NA) are dried at 110°C and 0.1 MPa for 12 h.

2.5. Sample characterization

XRD analysis is performed by a computerized Seifert 3000XRD diffractometer using Cu K α ($\lambda = 0.15406$ nm) radiation and a PW 2200 Bragg–Brentano $\theta/2\theta$ goniometer equipped with a bentgraphite monochromator and an automatic slit. Diffraction peaks are recorded in a 2θ range of 10–90° with step size of 0.033 and step scan of 10.0 s. Phase identification is carried out by comparison with database cards. The crystallite size of PHS nanoparticles is calculated from the full width at half maximum (FWHM) of the diffraction peaks using Debye–Scherer’s equation (Eq. (1)).

$$D = \frac{k\lambda}{\beta\cos\theta} \quad (1)$$

where, “D” is the average crystalline dimension perpendicular to the surface of the specimen, “ λ ” is the wavelength of used X-ray, “k” is Scherer’s constant (0.9), “ β ” is the full width at half maximum intensity of a Bragg reflection excluding instrumental broadening and “ θ ” is the Bragg diffraction angle. The values of the β and θ parameters from the XRD peak are estimated by Gaussian fitting.

A porous textural characterization of the synthesized samples is evaluated from the N₂ adsorption-desorption isotherms, determined at -196°C on an automatic apparatus Surfer sorption analyser (Thermo Scientific). The surface area of the samples is determined by the BET method using data from the adsorption isotherms in the range of relative pressures from 0.05 to 0.28 (for isotherms type IV). The total pore volume, known as volume of Gurvich, is determined based on the volume of adsorbate $V_{0.98}$, recorded on the desorption branch of the adsorption isotherm at a relative pressure (P_i/P_0) of 0.98. The micropore volume is calculated using the Dubinin-Radushkevich equation up to $P_i/P_0 \leq 0.15$. The pore diameters are obtained by applying the Non-local density functional theory (NLDFT) on N₂ adsorption data.

UV-vis spectra of the samples are recorded in the range of 200–800 nm at room temperature using a Thermo Evolution 300 UV-Vis spectrophotometer equipped with a praying mantis device. Spectralon is used as a reference material.

FT-IR spectra are recorded in the frequency region of 4000-400 cm^{-1} by means of a Nicolet iS 50 Thermo Scientific FT-IR spectrophotometer equipped with DTGS KBr detector (4 cm^{-1}) at scan's number of 32.

XPS analysis is carried out using ESCALAB MkII (VG Scientific) electron spectrometer at a base pressure in the analysis chamber of 5×10^{-10} mbar (during the measurement 10^{-8} mbar), using $\text{AlK}\alpha$ X-ray source (excitation energy 1486.6 eV). The pass energy of the hemispherical analyzer was 20 eV, 6 mm slit widths (entrance/exit). The instrumental resolution measured as the full width at a half maximum (FWHM) of the $\text{Ag}3d_{5/2}$, photoelectron peak is 1 eV. The energy scale is corrected to the $\text{C}1s$ – peak maximum at 285.0 eV for electrostatic charging. The processing of the measured spectra includes a subtraction of X-ray satellites and Shirley-type background [15]. The peak positions and areas are evaluated by a symmetrical Gaussian-Lorentzian curve fitting. The accuracy of the BE values was ± 0.2 eV. The relative concentrations of the different chemical species are determined based on normalization of the peak areas to their photoionization cross-sections, calculated by Scofield [16].

Thermal stability of the obtained samples is investigated by means of a thermal gravimetric analyzer Netzsch STA 449C. The experiment conditions are as follows: initial sample mass – 5.0mg, heating rates – $10^\circ\text{C}/\text{min}$, temperature range from 30 up to 700°C , nitrogen flow – 0.020 l/min, platinum pans. During the heating, variation of the weight loss with respect to time and temperature is collected automatically by the instrument. Differential scanning calorimetry (DSC) measurements are carried at the same experimental conditions.

2.6. Catalytic test

In a typical procedure, acetic acid (8.34 g, 0.1388 mol) and catalyst (10 wt.%, with respect to the mass of substrate) are placed in a three-necked round bottom flask of 0.100 l capacity. The latter is equipped with a condenser, a port for sample withdrawal and a thermometer. Mixing of the reaction fluids was performed by a magnetic stirrer. Once the desired reaction temperature (80°C) is reached, an equimolar amount (10.29 g, 0.1388 mol) of 1-butanol, separately heated to the set reaction temperature (80°C) is added into the reactor. This time is considered as zero reaction time ($t = 0$). The reaction progress is monitored by GC analysis. At regular intervals of time (10 min), a sample (1 ml) is withdrawn and immediately cooled in an ice bath. The reaction mixture is analyzed by GC

7890A (Agilent Technologies) equipped with a flame ionization detector and a capillary column HP-INNOWAX, 30 m×0.32 mm×0.25 μm. High purity helium at a flow rate of 0.0015 l/min is used as a carrier gas. The oven temperature is programmed at 70°C for 2 min and then it is raised from an initial value 70°C to 190°C at a ramp rate of 5°C/min. The injector and detector temperature are maintained at 250°C and 300°C, respectively. The analytical uncertainty of GC is less than 4%, which is in accordance with the acceptable limits. The acetic acid conversion is calculated according to Eq. (2). It should be noted that the occurrence of side reactions such as butylene synthesis due to alcohol dehydration is not registered.

$$X_A = \frac{C_{A_0} - C_A}{C_{A_0}} \quad (2)$$

where, X_A is acetic acid conversion, C_{A_0} is initial concentration (mol/l) of the acetic acid and C_A corresponds to the acetic acid concentration (mol/l) at a given reaction time (t , min).

3. Results and discussion

3.1. Phase composition and textural characterization

For a description of the crystalline phases present in the obtained supports and catalysts, a XRD analysis is conducted. The XRD patterns of Al-NA, RHA, PHS, PHS/Al-NA and PHS/RHA are presented in Fig. 1.

The X-ray diffraction analysis of Al-NA showed a number of strong XRD patterns at 2θ values of 25.50° ($d = 3.4965$), 35.12° ($d = 2.5532$), 37.68° ($d = 2.3854$) and 43.23° ($d = 2.0911$) which undoubtedly confirmed the presence of α -Al₂O₃ phase (ICDD No. 00-001-1296). The aforementioned 2θ values correspond to the (012), (104), (110) and (113) lattice planes of α -Al₂O₃, respectively [17]. It was established that our results completely coincide with those presented by other authors [18,19]. For example, electric field gradients and charge density in corundum, α -Al₂O₃ were established by Lewis et al. [19]. XDR analysis of the compound under investigation showed an appearance of strong peaks related to d-spacing values of 3.4913, 2.5545, 2.3910 and 2.0928. In another work, the thermal conductivity and viscosity of synthesized α -alumina-based nanofluids are investigated [20].

The authors report that the calcination temperature of 1100°C for 2 h results in the formation of a single-phase of corundum powder, being confirmed by XRD patterns at $2\theta = 25.71^\circ$, 35.18° , 38.90° and 43.44° . Except corundum, patterns (2θ values of 12.40° ($d = 7.1324$), 16.03° ($d = 5.5245$), 17.66° ($d = 5.0181$), 20.45° ($d = 4.3394$), 21.54° ($d = 4.1222$), 25.41° ($d = 3.5025$), 27.13° ($d = 3.2842$) and 29.07° ($d = 3.0693$) related to ammonium alum (ICDD No. 00-042-1430) were detected in the X-ray diffractogram of Al-NA as well. These are related to the (100), (102), (012), (011), (101), (110), (111) and (015) lattice planes of the $\text{NH}_4\text{Al}(\text{SO}_4)_2 \cdot 12\text{H}_2\text{O}$, respectively [21-24]. This indicates that a part of the ammonium alum has not been converted to corundum during the calcination process.

The X-ray diffraction analysis of the unsupported ionic liquid revealed strong peaks appeared at $2\theta = 10.43^\circ$ ($d = 8.4748$), 13.45° ($d = 6.5779$), 14.31° ($d = 6.1845$), 18.32° ($d = 4.8388$), 20.96° ($d = 4.2349$), 22.83° ($d = 3.8921$), 23.23° ($d = 3.8260$), 23.96° ($d = 3.7110$) and 24.59° ($d = 3.6174$), which correspond to the (010), (01 $\bar{1}$), (011), (002), (020), (1 $\bar{1}$ 1), (1 $\bar{1}$ $\bar{1}$), (11 $\bar{1}$) and (111) lattice planes, respectively. The registered XRD positions and the respective d-spacing values for the PHS sample in this paper are identical to those reported in a work of Rogers and Bauer [25], where the crystal structure of pyridinium hydrogen sulfate was presented for the first time. Indeed, for the aforementioned XRD patterns, d-spacing values of 8.4706, 6.5816, 6.1898, 4.8437, 4.2353, 3.8927, 3.8277, 3.7111 and 3.6184 are listed.

The X-ray patterns of the pure rice hush ash showed a typical broad diffraction peak in the range between 2θ of 13 and 40° with a maximum at 21.8° , which implies the presence of a high amount of an amorphous phase of silica (Fig. 1). Almost identical results can be found in different works, where an appearance of a broad diffraction peak around $2\theta = 22^\circ$ due to amorphous silica in RHA is clearly presented [26]. Except a phase of amorphous silica, the X-ray diffractogram of pure RHA in the current work contains a single XRD peak centered at $2\theta = 29.48^\circ$ ($d = 3.0275$). The latter is indication that a crystalline phase of calcite (ICDD No. 01-072-1652) present as a component in the synthesized RHA. Based on these results, it could be proposed that a number of Si-O-Ca interactions exist in pure RHA support. A XRD analysis of the crystalline calcium carbonate conducted by Harris et al. [27] showed a strong reflection at 2θ value of 29.50° , which corresponds to the (104) lattice plane in CaCO_3 .

Comparing the XRD profiles of the pure supports with the corresponding catalysts, significant alterations are detected (Fig. 1). The latter is much more pronounced in the case of PHS/Al-NA sample. Hence, the following phenomena are observed after impregnation of

Al-NA with the ionic liquid pyridinium hydrogen sulfate: (i) reflections, previously assigned to $\text{NH}_4\text{Al}(\text{SO}_4)_2 \cdot 12\text{H}_2\text{O}$ phase (12.40° , 14.31° , 16.03° , 17.66° , 21.54° and 27.73°), are no longer available in the XRD of PHS/Al-NA, (ii) diffraction peaks due to formation of new crystalline phases such as $(\text{NH}_4)_2\text{S}_2\text{O}_5$ (15.68° , 17.08° , 26.71° and 27.53° , ICDD No. 00-024-0012) and $\text{Al}_2(\text{SO}_4)_3$ (12.00° and 17.83° , ICDD No. 00-023-0767) are registered, (iii) presence of agglomerated PHS particles on the Al-NA surface is observed via appearance of XRD patterns at 2θ values of 10.42° , 22.84° and 24.59° and (iv) the XRD patterns (25.50° , 35.12° , 37.68° and 43.23°) characterizing corundum in Al-NA support are slightly decreased in intensity. Using Eq. (1), a value of 31.5 nm is calculated as an average size of the PHS particle on the Al-NA support surface. We believe that the observed phenomena are a consequence of a surface ionic liquid-support interaction, probably due to a formation of bonds between the oxygen atoms in the hydrogen sulfate anion and the metal ions in the $\text{NH}_4\text{Al}(\text{SO}_4)_2 \cdot 12\text{H}_2\text{O}$. In addition, a surface interaction between the aluminium sites (Al^{3+}) in $\alpha\text{-Al}_2\text{O}_3$ and the oxygen atoms in PHS should not be excluded as well.

Our statement that the $[\text{HSO}_4]^-$ fragment is mainly involved in the IL-support interaction is supported by a work of Sobota et al. [28], where the interaction mechanism of $[\text{C}_4\text{C}_1\text{Im}]^+[\text{Tf}_2\text{N}]^-$ on a well-ordered alumina surface is investigated. It is established that the $[\text{C}_4\text{C}_1\text{Im}]^+[\text{Tf}_2\text{N}]^-$ adsorbs in a slightly tilted orientation with respect to the surface, mainly interacting with the support via sulfonyl groups. In another paper, the surface interactions between $[\text{C}_4\text{C}_1\text{Im}]^+[\text{BF}_4]^-$ and $\gamma\text{-Al}_2\text{O}_3$ are studied [29]. Results reveal that the $[\text{BF}_4]^-$ anion is significantly polarized on the acidic Al^{3+} sites, while the $[\text{C}_4\text{C}_1\text{Im}]^+$ cation interacts with the superficial HO^- groups on the $\gamma\text{-Al}_2\text{O}_3$ surface. Guo and co-workers [30] impregnated Al_2O_3 with an acidic nitrate solution of $\text{ZrO}(\text{NO}_3)_2$ ($\text{pH} \leq 3$) and reported for a decreased crystallization degree of alumina due to breaking of the Al-O-Al bonds. Considering that the active phase in the current work is a Brønsted ionic liquid with a pK_A value of 3.2 [31], lower intensity of the characteristic XRD patterns for corundum in PHS/Al-NA sample in comparison with those in pure Al-NA carrier could be attributed to the acidic aqueous solution of IL (*see pt. 2.1.4*) used for Al-NA impregnation.

Results showed that the deposition of $[\text{H-Pyr}]^+[\text{HSO}_4]^-$ on RHA carrier does not affect the amorphous silica phase. However, the XRD peak ($2\theta = 29.48^\circ$) related to CaCO_3 phase in pure RHA cannot be detected in the XRD profile of PHS/RHA sample (Fig. 1). Instead of this, a crystalline phase of α -quartz (ICDD No. 01-070-2535) is registered by reflections at 2θ values of 25.42° ($d = 3.5011$), 35.95° ($d = 2.4961$), 38.56° ($d = 2.3329$), 41.06° ($d = 2.1970$) and 48.71° ($d = 1.8679$). These are related to the (101), (110), (102), (200) and (112) lat-

tice planes, respectively [32]. The observed results are trying to be explain using the above presented statement that the pure RHA contains oxygen atoms, linked to silicon and a charge balancing cation in the form of Si–O–Ca bonds. Knowing that the Si–O interaction (799.6 kJ/mol) is notably stronger than Ca–O (383.3 kJ/mol) [33], it could be assumed that during RHA impregnation with IL, the Ca ions will be removed easier than Si. In other words, a greater number of Si–O bonds is expected to present in the PHS/RHA sample in comparison with the number of Si–O bonds in RHA. However, IL-RHA surface interaction with the participation of Si atoms can be also proposed. A detailed analysis of the XRD profile of PHS/RHA revealed an absence of diffraction patterns related to PHS particles on the RHA surface. It proposes that the PHS particles are quite small to be identified by XRD. Taking into account that agglomerated PHS particles (31.5 nm) are registered on the Al-NA surface, it seems that the IL–Al-NA and IL–RHA interactions are different in nature.

In order to investigate the textural properties of the synthesized supports and catalysts, N₂ adsorption-desorption analysis (Fig. 2) is carried out. Results revealed that type IV-A isotherms characterize the obtained samples, according to the IUPAC classification [34]. Type IV isotherms are usually given by mesoporous materials, where the mechanism of adsorption of simple gasses (such as nitrogen) begins with the formation of a monolayer on the surface, followed by multilayer formation and finally by capillary condensation [35]. In the case of a type IV-A isotherm, the capillary condensation is accompanied by hysteresis loop. For the samples studied in the current work, type H-1 hysteresis is registered. The latter is found in materials which exhibit a narrow range of uniform mesopores [36].

A detailed analysis of the textural properties of the pure supports showed that a value of 71 m²/g characterizes the specific surface area (S_{BET}) of Al-NA (Table 1). In this regard, almost identical S_{BET} (78 m²/g) is obtained in the case of RHA carrier. However, the total pore volume (V_{total}) of the Al-NA sample (0.5532 cm³/g) is found to be 2.27 times higher than that (0.2436 cm³/g) of RHA. It is correlated to the significantly larger volume (0.5258 cm³/g) of the mesopores of Al-NA with respect to the volume (0.2161 cm³/g) of the mesopores in RHA. For comparison, the volume (0.0274 cm³/g) of the micropores in the Al-NA and RHA (0.0276 cm³/g) carriers is practically identical.

N₂ adsorption-desorption analysis established that both the specific surface area and the total pore volume of the pure supports are notably decreased after the ionic liquid deposition. For example, S_{BET} of PHS/Al-NA and PHS/RHA is established to be 4 and 2 m²/g, respectively. In addition, values of 0.0269 and 0.0083 cm³/g are found as V_{total} for the PHS/Al-NA and PHS/RHA, respectively. These effects are manly attributed to the plugging

of the support pores with PHS species. It is interesting to point out that the difference (3.24 times) between the V_{total} of the PHS/Al-NA and PHS/RHA is greater than that (2.27 times) between V_{total} of the corresponding supports. This assumes that the plugging may not be the only reason for the registered V_{total} difference. It was already showed that the PHS phase on the RHA surface is much more dispersed in comparison with those on the Al-NA. Therefore, the difference between V_{total} of the PHS/Al-NA and PHS/RHA samples could be also attributed to a process of pores filling (being observed in a greater extent in the case of PHS/RHA sample), occurring simultaneously with the pores plugging.

3.2. Surface analysis

In the previous subsection was observed that the PHS particles on the RHA carrier are significantly smaller than those on the Al-NA surfaces, which allowed us to state that the PHS-RHA and PHS-Al-NA interactions are different in nature. To clarify this, the surface effects on the PHS/RHA and PHS/Al-NA are studied via FT-IR and XPS. Infrared spectra of the PHS/RHA and PHS/Al-NA samples in the regions $400\text{-}900\text{ cm}^{-1}$ and $950\text{-}3800\text{ cm}^{-1}$ are presented in Fig. 3. For comparison the FT-IR profiles of Al-NA, RHA and PHS are added as well. It should be pointed out that a detailed FT-IR analysis on the PHS sample was carried out in a previous our work [37]. Nevertheless, for a better understanding the PHS-RHA and PHS-Al-NA interactions, a brief discussion on the vibrational modes in PHS is present in the current work as well.

3.2.1. Vibrational assignments in the pure supports and ionic liquid

FT-IR spectrum of the Al-NA support showed that well-defined infrared bands appear at wavenumber values of 445.4 (bending Al-O), 502.4 (octahedral coordinated aluminium of AlO_6), 588.3 (Al-O stretching), 615.1 (Al-O stretching) and 632.1 cm^{-1} (stretching Al-O-Al), related to vibrational modes in $\alpha\text{-Al}_2\text{O}_3$ [38]. It was found that our observations correspond well with these presented by Boumaza et al. [39], where the specific signatures of corundum powders by FT-IR spectroscopy are investigated. The authors reported that FT-IR spectrum of corundum contains infrared bands at 447, 594 and 640 cm^{-1} due to Al-O vibrational modes.

Except infrared bands between 400 and 635 cm^{-1} , absorbance of very low intensity at 736.6 and 830.3 cm^{-1} is also registered in the FT-IR spectrum of Al-NA. The first one is due to a torsional Al-O mode, while the second one expresses N-S bond [40]. These results

completely coincide with the XRD analysis, where a phase of ammonium alum is registered in the Al-NA carrier. Another conformation for the presence of $\text{NH}_4\text{Al}(\text{SO}_4)_2 \cdot 12\text{H}_2\text{O}$ is obtained by the infrared bands at 1094.9, 1161.3 (shoulder), 1237.5 (shoulder), 1397.9 and 1447.1 cm^{-1} . The bands between 1090 and 1240 cm^{-1} characterize the S–OH and S=O vibrations in sulfate groups (SO_4^{2-}) [41], while that at 1397.9 cm^{-1} is related to ammonium cations (NH_4^+) [42]. In addition, the absorbance at 1447.1 cm^{-1} is recognized as N–H deformation vibrations in NH_4^+ . The infrared bands at wavenumber values of 1635.4 and 3418.4 cm^{-1} indicates O–H bending and stretching vibrations, respectively, due to water [43]. It is interesting to point out that the FT-IR spectrum of Al-NA contains bands at 2468.3 and 2921.3 cm^{-1} , correlated to impurities, adsorbed on the support surface. Hence, the band at 2468.3 cm^{-1} is assigned to CO_3^{2-} species [37], whereas the second one is an indication for carbonaceous residues (C–H) linked to the alumina network skeleton [44].

The vibrational spectrum of RHA carrier between 400 and 900 cm^{-1} revealed infrared bands at wavenumber values of 465.6, 572.2, 797.8 and 873.4 cm^{-1} . The strong absorption peaks at 465.6 (asymmetric Si–O–Si bending modes) and 797.8 cm^{-1} (symmetric Si–O–Si stretching modes) represent amorphous silica [45], while the infrared bands at 572.2 (symmetric CO_3^{2-} deformations) and 873.4 cm^{-1} (asymmetric CO_3^{2-} deformations) correspond to CaCO_3 [46]. These findings support the XRD results (Fig. 1), where amorphous silica and calcite phases in the RHA samples are detected.

Analyzing the FT-IR spectrum of RHA in the region above 900 cm^{-1} , additional infrared peaks due to silica and calcite phases are registered. For instance, the intensive absorption band at 1092.2 cm^{-1} with two well-defined shoulders at 960.6 and 1223.3 cm^{-1} are referred as asymmetric Si–O–Si stretching band, stretching mode of Si–OH and symmetric Si–O–Si stretching vibration, respectively [47]. The presence of CaCO_3 in the RHA carrier is also confirmed by a peak of low intensity at wavenumber value of 1424.6 cm^{-1} , attributed to asymmetric CO_3^{2-} stretching mode [46]. Signatures of water (1637.9 and 3436.9 cm^{-1}) [43] and adsorbed carbonaceous residues (2923.2 cm^{-1}) [44] are registered in the FT-IR spectrum of RHA as well. These are established to be less pronounced in the RHA spectrum in comparison with the respective ones in the case of Al-NA support.

FT-IR spectrum of the unsupported pyridinium hydrogen sulfate in the low-frequency region (400-900 cm^{-1}) showed infrared peaks at 455.4 and 748.9 cm^{-1} which represent bending and stretching vibrations in the SO_4^{2-} group, respectively [48]. The absorbance at 586.3 and 840.6 cm^{-1} is correlated to a stretching O···H vibration between the pyridinium cation and the $[\text{HSO}_4]^-$ fragment [37]. The bands at wavenumber values of 621.7, 677.9 and

879.4 cm^{-1} is related to C=C and N=C vibrations in the aromatic ring [49]. Additional infrared bands due to stretching S–O vibrations in the PHS sample are registered in the region above 950 cm^{-1} , namely 1002.3, 1171.5 and 1322.3 cm^{-1} . In light of this, the peak at 1047.6 cm^{-1} and those from 1480 to 1620 cm^{-1} are characteristic for stretching C=C and N=C vibrations in the [H–Pyr]⁺ cation.

Purely stretching C–H modes in the aromatic ring are detected at wavenumber values between 3000 and 3230 cm^{-1} [50]. An indication for protonated pyridine in PHS structure is obtained via infrared bands at 1457.2, 1631.8 and 2850.9 cm^{-1} , assigned to N–H vibrations [40,41]. It should be noted that the band at 1631.8 cm^{-1} is notably broaden, probably due to a presence of vibrational O–H mode component in the form of N–H \cdots O–S interaction between [H–Pyr]⁺ and [HSO₄]⁻ moieties in PHS. A stretching O–H vibration in water is recognized at 3409.3 cm^{-1} .

3.2.2. Vibrational assignments in PHS/Al-NA and PHS/RHA samples

Results showed that the intensity of the IR bands at 445.4, 502.4 and 632.1 cm^{-1} , previously assigned as vibrational modes in α -Al₂O₃, slightly decrease when the ionic liquid is immobilized on the Al-NA surface. In the same way, the peak intensity at 748.9 cm^{-1} (stretching SO₄²⁻ vibration in pure PHS) is notably decreased in the spectrum of PHS/Al-NA. Consequently, a surface interaction between the Al³⁺ sites in Al-NA support and the O atoms in [HSO₄]⁻ is proposed. In other words, a greater number of Al–O bonds in the PHS/Al-NA sample with respect to that in the pure support should be expected. This statement is confirmed by the peak at 615.1 cm^{-1} (related to stretching Al–O vibration) in the spectrum of PHS/Al-NA, which is found to be more pronounced in comparison with the same band in the IR spectrum of pure Al-NA.

On the other hand, the infrared pattern at 1171.5 cm^{-1} in the spectrum of PHS undergoes a considerable red shift to 1094.6 cm^{-1} in the spectrum of PHS/Al-NA. As a result, it completely coincides with the position of the band in pure Al-NA, characterizing SO₄²⁻ groups in the form of NH₄Al(SO₄)₂·12H₂O. Furthermore, the intensity of the band at 1094.6 cm^{-1} in the PHS/Al-NA spectrum is notably higher than that in the spectrum of pure Al-NA support. Based on the aforementioned effects, we assumed that a surface interaction (Al–O–S) between the metal ions in NH₄Al(SO₄)₂·12H₂O and the hydrogen sulfate anion has occurred during the impregnation process.

It is interesting to point out that the absorption band at 1447.1 cm^{-1} (recognized as deformation N–H vibrations in NH_4^+) does not present in the IR spectrum of PHS/Al-NA. Instead of this, the IR pattern at wavenumber value of 1397.9 cm^{-1} (free NH_4^+) in pure Al-NA support possesses a higher intensity when the ionic liquid is immobilized on the Al-NA surface. Considering that new phases of $(\text{NH}_4)_2\text{S}_2\text{O}_5$ and $\text{Al}_2(\text{SO}_4)_3$ present in the PHS/Al-NA structure (*see pt. 3.1*), it could be proposed that a cleavage of chemical bonds in the ammonium alum structures is responsible for the increased intensity of the IR band at 1397.9 cm^{-1} . We assumed that the formation of $(\text{NH}_4)_2\text{S}_2\text{O}_5$ and $\text{Al}_2(\text{SO}_4)_3$ phases is connected with surface IL-support interactions in the form of Al–O–S and N–H \cdots O–S bonds. The O–S component in these bonds expresses the $[\text{HSO}_4]^-$ from the IL, while the Al and N–H denotes the Al^{3+} and NH_4^+ sites, respectively, in the Al-NA carrier structure.

Except a support-anion interaction (expressed as Al–O–S and N–H \cdots O–S bonds) the FT-IR spectrum of the PHS/Al-NA sample revealed that the pyridinium cation might be involved in the overall PHS–Al-NA surface interaction as well. For example, the infrared band at 586.3 cm^{-1} (denoted as stretching vibration of O \cdots H bond between $[\text{H-Pyr}]^+$ and $[\text{HSO}_4]^-$ moieties) in the spectrum of pure PHS cannot be clearly observed in the spectrum of Al-NA supported ionic liquid. Moreover, it was established that the IR pattern at 588.6 cm^{-1} (related to Al–O vibration in corundum) decreases in intensity when the PHS/Al-NA sample is obtained. Considering these results, we stated a cleavage of the S–O \cdots H–N bond in pure PHS during impregnation and formation of a new hydrogen bond (Al–O \cdots H–N) between the Al^{3+} sites in Al-NA support and the N atom in $[\text{H-Pyr}]^+$ cation. Knowing that the atomic radius of aluminium (0.125 nm) is higher than that of sulfur (0.100 nm) [51], it could be assumed that the Al–O interaction in the Al–O \cdots H–N bond (PHS/Al-NA sample) will be less pronounced in comparison with the S–O interaction in the S–O \cdots H–N bond (pure PHS sample). In other words, the oxygen atom in Al–O \cdots H–N should possess a higher electron density with respect to the oxygen atom in S–O \cdots H–N. As a result, the N–H bond in the PHS/Al-NA is expected to be more suppressed than the same bond in the pure PHS. An evidence for the latter is a higher intensity of the IR bands at 1457.2 , 1631.8 and 2850.9 cm^{-1} , (assigned to N–H vibrations in pure PHS), than the intensity of the same bands in the spectrum of PHS/Al-NA. Unlike intensity, the position of the bands characterizing the N–H vibrations in pure PHS does not differ after the Al-NA impregnation with ionic liquid. Therefore, the interactions S–O \cdots H–N (in pure PHS) and Al–O \cdots H–N (in PHS/Al-NA) are referred as very similar in nature.

A detailed analysis on the FT-IR spectrum of the Al-NA supported pyridinium hydrogen sulfate revealed that the bands in the region from 3000 to 3200 cm^{-1} (C-H vibrations) is significantly reduced in intensity in comparison with the same bonds in the spectrum of pure PHS. In addition, the IR band at 1631.8 cm^{-1} (mixed N-H and O-H vibrations) in the spectrum of Al-NA supported ionic liquid is notably wider in comparison with the same bond in pure PHS. Hence, it is proposed that the support-cation interaction is not limited to the formation of Al-O \cdots H-N bond and the carbon atoms in the aromatic ring are involved as well. Based on the above presented results, we suggested that an additional hydrogen bond in the form of C-H \cdots O-Al interaction exists in the interface between pure PHS and Al-NA support.

Similar to the bands between 3000 and 3200 cm^{-1} , the absorbance at wavenumber value of 677.9 cm^{-1} (C=C vibrations) in PHS/Al-NA also possesses a lower intensity with respect to the same band in the spectrum of pure PHS. Moreover, the IR pattern at 879.4 cm^{-1} (observed in PHS) practically does not present in the spectrum of PHS/Al-NA. In contrary, a well-defined infrared peak at 1254.6 cm^{-1} appears in the IR spectrum of PHS/Al-NA sample. According to the literature data, the IR absorbance around 1250 cm^{-1} is a typical stretching vibration of a single C-O bond [52]. Thus, we believe that the peak at 1254.6 cm^{-1} in the IR spectrum of PHS/Al-NA is a consequence of cation-anion interaction in the supported PHS due to formation of C-O-S bond. It should be noted that a similar interaction (C \cdots O-S) was observed in the pure PHS and it was denoted as strongly electrostatic in nature [31]. The latter correlates well the IR spectrum of pure PHS, where a IR band due to a stretching C-O vibration is hard to be found. The clearly registered band at 1254.6 cm^{-1} in the IR spectrum of PHS/Al-NA implies that the distance between [H-Pyr] $^+$ and [HSO $_4$] $^-$ fragments considerably decreases after the IL immobilization on the Al-NA. It agrees in some extent with the XRD analysis, where a phase of agglomerated PHS particles was registered on the Al-NA carrier surface.

The vibrational spectrum of PHS/RHA sample indicated that the IR band at 465.6 cm^{-1} (bending Si-O-Si modes in pure RHA) notably decreases and completely overlaps the absorbance pattern at 455.4 cm^{-1} (vibrations of the SO $_4^{2-}$ group in pure PHS). In addition, the band at 797.8 cm^{-1} (stretching Si-O-Si modes in pure RHA) is almost disappeared when the IL is immobilized on the RHA surface. These findings are attributed to a support-anion interaction via formation of Si-O-S bonds. Similar effects are registered in the PHS/RHA spectrum between 950 and 1230 cm^{-1} , where the bands (960.6, 1092.2 and 1223.3 cm^{-1}) in the spectrum of pure RHA and those (1002.3 and 1171.5 cm^{-1}) in the spectrum of pure PHS

appear as a double peak, correlated to stretching modes of Si–O and S–O bands which are overlapped together.

It is worth noting that the absorbance bands (621.7 , 677.9 and 879.4 cm^{-1}) related to vibrations in the aromatic ring of PHS are notably decreased in intensity after the IL immobilization of RHA. However, these bands are still well-defined (regardless of their low intensity) in the IR spectrum of PHS/RHA. Lower intensity of the aforementioned patterns in PHS/RHA with respect to their intensity in PHS is associated with a surface support-cation interaction, similar to that presented earlier in the case of PHS/Al-NA sample. The fact that the IR spectrum of PHS/RHA follows the IR profile of the pure ionic liquid (Fig. 3) could be interpreted as a RHA surface which is significantly covered by PHS species. The latter corresponds with the XRD of PHS/RHA, where the presence of highly dispersed PHS particles on the RHA is assumed. A conformation that the PHS–RHA interaction is stronger than PHS–Al-NA is obtained comparing the IR spectra of PHS/RHA and PHS/Al-NA in the region above 1430 cm^{-1} . Hence, the absorption bands in the spectrum of PHS/RHA are found to be more suppressed (expressed by their lower intensity) than the same bonds in the IR spectrum of PHS/Al-NA. Another important effect in the IR spectrum of PHS/RHA is the absence of the absorption bands at 572.2 , 873.4 and 1424.6 cm^{-1} , previously connected with CO_3^{2-} vibrations of calcite in pure RHA. The latter agrees well with the XRD data, where no CaCO_3 phase is registered in PHS/RHA.

3.2.3. Core-electron levels description

In order to confirm the XRD and FT-IR results, XPS analysis of the pure carriers and the corresponding supported ionic liquid is carried out. XPS of O 1s, C 1s, N 1s, Al 2p and S 2p, core-electron levels for Al-NA and PHS/Al-NA are presented in Fig. 4. In this regard, XPS of O 1s, C 1s, N 1s, Si 2p, S 2p and Ca 2p core-electron levels for RHA and PHS/RHA are presented in Fig. 5. In addition, the surface atomic concentrations of the elements in the investigated samples are depicted in Table 2.

Results showed that the O 1s spectrum of pure Al-NA support contains three components with binding energy (BE) values of 530.6 , 531.7 and 533.2 eV. The first component is attributed to lattice O^{2-} species [53], most probably in corundum and ammonium alum structures. The second one (531.7 eV) correspond to a surface oxygen in SO_4^{2-} [54] and Al–O [55] environment, while the component with the highest BE expresses oxygen-containing species in the form of hydroxyl (O–H) groups [56]. However, the O 1s profile of pure Al-NA

carrier differs when pyridinium hydrogen sulfate is immobilized on the Al-NA surface. In details, the fragments with BE of 530.6 and 533.2 eV are not observed in the O 1s spectrum of PHS/Al-NA but only a single peak at 531.5 eV. Obviously, the position of the latter is practically identical to that (531.7) of the O 1s peak associated with SO_4^{2-} and Al-O in pure Al-NA. These results coincide with the XRD, where a transformation of $\text{NH}_4\text{Al}(\text{SO}_4)_2 \cdot 12\text{H}_2\text{O}$ phase into $(\text{NH}_4)_2\text{S}_2\text{O}_5$ and $\text{Al}_2(\text{SO}_4)_3$ is observed. On the other hand, the data presented in Table 2 revealed that the oxygen concentration on the Al-NA (55 at.%) and PHS/Al-NA (53 at.%) surfaces does not differ. Based on this, it could be proposed: (i) absence of lattice oxygen migration to the Al-NA surface during impregnation and/or (ii) formation of agglomerated PHS particles on the Al-NA.

Analyzing the O 1s line of pure RHA support (Fig. 5), two components with a binding energy of 530.6 and 532.8 eV due to Ca-O in calcite [57] and Si-O-Si unit [58], respectively, are observed. Although the position of the intensive peak at 532.8 eV is typical for Si-O-Si group, the presence of Si-O-Ca fragment due to the relative electronegativities of the component elements should not be excluded. Silicon is more electronegative than calcium, thus the oxygen atom experiences decreased atomic shielding and has a high binding energy. The presence of calcite phase in the pure RHA carrier (also observed by FT-IR and XRD) is confirmed by appearance of a doublet peak of Ca $2p_{1/2}$ (351.3 eV) and Ca $2p_{3/2}$ (347.6 eV) with a spin-orbit splitting of 3.7 eV (Fig. 5), which is representative of Ca^{2+} in CaCO_3 [59].

The ionic liquid deposition on the RHA carrier caused the low-intensive O 1s peak due to Ca-O (and/or Si-O-Ca) and these related to Ca^{2+} (Ca $2p_{1/2}$ and Ca $2p_{3/2}$) to be not detected in the XPS spectrum of PHS/RHA sample. These effects completely agree with the XRD and FT-IR studies, where a phase of CaCO_3 in the RHA supported ionic liquid is not distinguished. On the other hand, the dominant peak (532.8 eV) in pure RHA is shifted to a binding energy value of 531.7 eV in the spectrum of PHS/RHA, which is 0.9 eV lower than Si-O-Si binding energy. The appearance of the peak at BE of 531.7 eV is recognized as Si-O bonds formation [60] due to loss of a bond with oxygen atom in the first neighbor or the changes in the second neighbors. Therefore, it can be concluded that Si-O-Si covalent bonds in the RHA support are broken during the PHS/RHA synthesis. This confirms the FT-IR investigation, where the infrared bands at 465.6 and 797.8 cm^{-1} (related to Si-O-Si modes in pure RHA) are notably decreased when PHS is immobilized on the support surface.

XPS analysis showed that the surface oxygen concentration on the pure RHA is reduced with 15% (from 60 to 51 at.%) when the PHS/RHA sample is obtained (Fig. 5, Table 2). Different reasons could be introduced as a possible explanation: (i) removing of the CaCO_3 phase during the RHA impregnation with pyridinium hydrogen sulfate, which lowers the surface oxygen content and (ii) a significant amount of PHS species present on the support surface. The latter implies a predominant formation of Si–O–S bonds between PHS and RHA, being already registered by FT–IR. However, knowing that only 2 at.% characterizes the Ca^{2+} concentration on the pure RHA surface (Table 2), we assumed that PHS particles present on the RHA surface are mainly responsible for decreased surface oxygen concentration on the PHS/RHA carrier in comparison with that on RHA.

Comparing the oxygen concentrations of PHS/Al-NA (53 at.%) and PHS/RHA (51 at.%) surfaces, it can be seen that these are almost identical. However, the XRD study clearly demonstrated that the PHS particles present on the RHA surface are significantly smaller in size in comparison with these on Al-NA. This implies that a greater number of O-containing sites (expressed by $[\text{HSO}_4]^-$ fragments in IL) should present on the PHS/RHA surface with respect to that on Al-NA supported ionic liquid. To explain this contradiction, we proposed that during the RHA impregnation with an ionic liquid, a number of the PHS species are situated perpendicular to the support surface. As a result, $[\text{H-Pyr}]^-$ moieties in the immobilized IL are predominantly registered by XPS. It correlates with the oxygen concentration on the RHA surface which was found to be lower than that on PHS/RHA. The statement that a number of PHS species are probably placed perpendicular to the RHA surface is confirmed to some extent comparing the C 1s profiles of PHS/Al-NA and PHS/RHA (see below).

Another indication that the PHS particles on the RHA surface possess a smaller size than these on Al-NA and is obtained by analysis of the C 1s, S 2p and N 1s core-electron levels for PHS/Al-NA (Fig. 4) and PHS/RHA (Fig. 5) samples. Prior to that, the corresponding core-electron levels for pure supports are described. Hence, the XPS investigation showed that C 1s spectrum of Al-NA carrier contains peaks centered at 287.6 and 285.1 eV, related to C=O and C–C/C–H groups, respectively [61]. It agrees well with the FT–IR study of Al-NA (Fig. 3), where bands at 2468.3 and 2921.3 cm^{-1} assigned to adsorbed impurities are detected. In this regard, the C 1s line of RHA also showed presence of carbonaceous residues (C–C/C–H). However, a component at BE of 289.2 eV due to O–C=O in calcite is detected [59], in accordance with the XRD and FT–IR analyses. It should be noted that the carbon concentration on the Al-NA surface is about 17% more pronounced than that on the RHA support (Table 2). This supports the FT–IR data, where the infrared bands between 2800

and 3200 cm^{-1} in the spectrum of Al-NA sample are established to be more intensive in comparison with same bands in the spectrum of RHA. The IL deposition on Al-NA and RHA caused the peaks at 287.6 and 289.2 eV to be not present in the C 1s spectra of PHS/Al-NA and PHS/RHA, respectively. Moreover, the peak at BE value of 285.1 eV increased considerably in intensity. The latter was especially noticeable in the case of RHA supported PHS, where the surface carbon concentration is found to be more than 40% higher than that on the PHS/Al-NA. This assumes that the RHA possesses a greater number of exposed PHS particles in comparison with Al-NA due to a stronger IL-RHA surface interaction.

We came to the same conclusion, evaluating the S 2p core-electron level. Thus, the S 2p line of pure Al-NA (Fig. 4) showed two characteristic doublets at BE values of 170.1 (S $2p_{1/2}$) and 168.8 eV (S $2p_{3/2}$) (Fig. 5), which are typical for SO_4^{2-} groups [62]. This is in accordance with XRD and FT-IR analyses, where presence of sulfate groups in Al-NA sample (due to $\text{NH}_4\text{Al}(\text{SO}_4)_2 \cdot 12\text{H}_2\text{O}$ phase) was detected. It was found that the aforementioned doublets considerably increase in intensity and slightly shift towards lower BE values (from 170.1 to 169.8 eV and from 168.8 to 168.5 eV, respectively) after the Al-NA impregnation with PHS. The first effect could be related to the presence of additional sulfate-containing phase (such as $[\text{H-Pyr}]^+[\text{HSO}_4]^-$) on the Al-NA surface. Considering that the BE difference (0.3 eV) between S 2p core-electron levels of pure Al-NA and PHS/Al-NA is not noticeable, a weak surface IL-support interaction and/or SO_4^{2-} in a slightly different environment should be expected in that case. Earlier, the XRD data revealed agglomerated PHS particles and $(\text{NH}_4)_2\text{S}_2\text{O}_5$ and $\text{Al}_2(\text{SO}_4)_3$ phases in PHS/Al-NA. Results showed that binding energy values of 169.2 and 167.9 eV characterize the S $2p_{1/2}$ and S $2p_{3/2}$, respectively in the case of PHS/RHA (Fig. 5), which is 0.6 eV lower than the corresponding ones for PHS/Al-NA. It is connected with a stronger IL-RHA interaction (via Si-O-S bonds formation) in comparison with the IL-Al-NA one (expressed by Al-O-S connections). It is interesting to point out that the sulfur concentration on the PHS/Al-NA and PHS/RHA surfaces are strongly equivalent (Table 2). This seems to contradict the XRD, where the sulfate-containing phases ($(\text{NH}_4)_2\text{S}_2\text{O}_5$, $\text{Al}_2(\text{SO}_4)_3$, $[\text{H-Pyr}]^+[\text{HSO}_4]^-$) in PHS/Al-NA assume a higher sulfur concentration on the PHS/Al-NA surface than that on PHS/RHA. Hence, a greater number of PHS sites on the RHA surface (due to stronger IL-support interaction) with respect to these on Al-NA was supposed to clarify this discrepancy.

Figures 4 and 5 exposed that the N 1s core-electron level of PHS/Al-NA and PHS/RHA is presented as a single peak at 401.1 and 400.9 eV, respectively, connected with a protonated nitrogen in the form of C-N⁺ and/or NH₄⁺ [63]. Although a more dispersed PHS phase is

proposed on the RHA surface, the nitrogen concentration on PHS/Al-NA is found to be identical to that on the RHA supported ionic liquid (Table 2). It is connected with the presence of increased amount of NH_4^+ species on the Al-NA surface during impregnation, being registered by FT-IR. Indeed, the band at 1397.9 cm^{-1} in the infrared spectrum of PHS/Al-NA sample is observed to be more intensive than the same band in the IR spectrum of pure Al-NA support.

Similar to the N 1s core-electron level, the Al 2p line of pure Al-NA carrier is expressed as a single peak as well (Fig. 4). Since the registered BE value of 74.3 eV correspond to aluminium species in octahedral coordination [53], the Al 2p peak characterizes the aluminium in $\alpha\text{-Al}_2\text{O}_3$ and $\text{NH}_4\text{Al}(\text{SO}_4)_2 \cdot 12\text{H}_2\text{O}$ phases [64]. While minor changes in the Al 2p peak position (74.1 eV) are observed after the Al-NA carrier impregnation with pyridinium hydrogen sulfate, the aluminium concentration on the PHS/Al-NA surface is significantly reduced (from 37 to 22 at.%) in comparison with that on pure support (Table 2). Based on the first effect, it could be assumed that the aluminium environment in Al-NA does not differ notably from that in PHS/Al-NA. This is associated well with the XRD study, where a phase transformation of $\text{NH}_4\text{Al}(\text{SO}_4)_2 \cdot 12\text{H}_2\text{O}$ into $(\text{NH}_4)_2\text{S}_2\text{O}_5$ and $\text{Al}_2(\text{SO}_4)_3$ is detected. On the other hand, lower surface Al concentration in Al-NA supported ionic liquid proposed that the Al-NA surface is considerably covered by PHS particles, being already detected by FT-IR.

Results showed that the effects in the RHA and PHS/RHA samples analyzed by Si 2p core-electron level (Fig. 5) are identical to those described earlier by means of the corresponding O 1s lines. For example, the component at BE of 103.6 eV in the Si 2p spectrum of pure RHA corresponds to Si^{4+} (expressed as Si-O-Si bonds) in silica [65]. However, both the binding energy and the intensity of this component decreased notably when the PHS/RHA is synthesized. As a result, a peak with a BE value of 102.7 eV due to Si-O interaction is registered. In accordance with the Al 2p analysis described above, reduced intensity of the Si 2p peak for RHA supported ionic liquid can be associated with the presence of PHS species on the RHA surface. Comparing the surface Si and Al concentrations on the pure supports with the corresponding catalysts (Table 2), it can be clearly seen that the first one decreases in a greater extent (50%) with respect to Al (40%). It implies that that a greater number of PHS particles present on the RHA surface in comparison with Al-NA one. In other words, a higher PHS dispersion on the RHA is observed, supporting the XRD and FT-IR studies.

3.3. Electronic transitions

Electronic spectra of the obtained Al-NA, RHA, PHS, PHS/Al-NA and PHS/RHA samples are presented in Fig. 6. Following the above used model of discussion, the electronic transitions in the pure supports and ionic liquid are described first.

Results showed that the UV-vis spectrum of Al-NA carrier contains absorption bands at wavelength values of 245, 280, 311 and 357 nm, which are attributed to the charge transfers $\text{SO}_4^{2-} \rightarrow \text{Al}^{3+}$ [66], $\text{O}^{2-} \rightarrow \text{Al}^{3+}$ [67], $\text{SO}_4^{2-} \rightarrow \text{NH}_4^+$ [68] and $\text{OH}^- \rightarrow \text{Al}^{3+}$ [69], respectively. Analyzing the electronic spectrum of RHA, absorption bands due to electron density distributions $\text{CO}_3^{2-} \rightarrow \text{Ca}^{2+}$ (231 and 359 nm) [70] and $\text{O}^{2-} \rightarrow \text{Si}^{4+}$ (298 nm) [71] are detected, respectively. Obviously, these assignments agree with the XDR, FT-IR and XPS studies, where corundum and ammonium alum phases are registered in Al-NA. In addition, calcite and silica are clearly observed in the RHA.

Considering that the ionic liquid pyridinium hydrogen sulfate is composed by an organic ([H-Pyr]⁺) and an inorganic ([HSO₄]⁻) fragments, different electronic transitions are expected to present in this structure. Hence, to describe the origin of these charge transfers, the experimental wavelengths are compared with theoretical ones. For that purpose, the theoretical UV-vis spectrum of PHS (added as a supporting material, Fig. 1S) is computed as a vertical electronic excitation energy from the minima of the ground-state structure (added as a supporting material, Fig. 2S) in a condensed phase (water) via a time-dependent density functional theory [72] using a conductor-like polarizable continuum model [73].

The electronic spectrum of pure ionic liquid possesses a typical shape of protonated pyridine [74], containing absorption peaks at 207, 239, 245, 250, 255 and 263 nm. As will be shown later, the bands in the region 200-250 nm are due to $\pi \rightarrow \pi^*$ transitions, while these from 250 to 270 represent $n \rightarrow \pi^*$ charge transfers [75]. The corresponding theoretical wavelength values are calculated at 209, 227, 229, 230, 246 and 275 nm, respectively. For a detailed analysis of the electronic transitions in the PHS, frontier molecular orbitals for six excited states are studied. The frontier molecular orbitals which are active in the electronic absorption spectrum of PHS are HOMO, HOMO-1, HOMO-2, HOMO-3, LUMO and LUMO+1. The theoretical analysis revealed that HOMO and HOMO-1 are strongly delocalized on the oxygen atoms in the [HSO₄]⁻ moiety as the contribution $\psi_{\text{HOMO}} = 14.4\% 3p_y(\text{O}^5) + 11.1\% 4p_y(\text{O}^5) + 10.6\% 3p_x(\text{O}^4) + 8.3\% 4p_x(\text{O}^4) + 7.2\% 2p_y(\text{O}^5) - 6.5\% 3p_x(\text{O}^3)$ and $\psi_{\text{HOMO-1}} = 12.5\% 3p_z(\text{O}^3) + 10.0\% 4p_z(\text{O}^3) - 8.4\% 3p_x(\text{O}^2) - 8.0\% 3p_z(\text{O}^5) - 6.6\% 4p_z(\text{O}^5) + 6.4\% 3p_x(\text{O}^5)$. It could be seen that HOMO is expressed by p_y and p_x orbitals of the oxygen

atoms, while p_z orbitals characterize HOMO-1. In the opposite case, LUMO and LUMO+1 are completely delocalized on the pyridinium ring in PHS as the contribution $\psi_{\text{LUMO}} = 12.8\% 3p_z(\text{C}^{10}) + 9.9\% 4p_z(\text{C}^{10}) + 9.7\% 3p_z(\text{N}^{13}) - 6.5\% 4p_z(\text{C}^8) - 6.5\% 3p_z(\text{C}^8) + 6.5\% 2p_z(\text{C}^{10})$ and $\psi_{\text{LUMO}+1} = 9.6\% 3p_z(\text{C}^9) - 9.4\% 3p_z(\text{C}^{11}) + 8.5\% 3p_z(\text{C}^{12}) + 8.3\% 4p_z(\text{C}^9) - 8.3\% 3p_z(\text{C}^8) - 8.1\% 4p_z(\text{C}^{11})$. It is exposed that HOMO-2, HOMO-3 are mainly delocalized on the O atom in the hydrogen sulfate anion as the contribution $\psi_{\text{HOMO}-2} = -9.7\% 3p_z(\text{O}^4) - 7.7\% 4p_z(\text{O}^4) - 5.8\% 3p_z(\text{C}^8) + 5.7\% 3p_z(\text{C}^{12}) + 5.0\% 3p_z(\text{C}^{11}) - 4.8\% 2p_z(\text{O}^4)$ and $\psi_{\text{HOMO}-3} = -8.5\% 3p_z(\text{O}^4) - 6.9\% 4p_z(\text{O}^4) - 6.2\% 3p_z(\text{C}^{12}) + 6.0\% 3p_z(\text{C}^8) + 5.1\% 3p_z(\text{C}^9) - 4.9\% 3p_z(\text{C}^{11})$. However, the $\psi_{\text{HOMO}-2}$ and $\psi_{\text{HOMO}-3}$ demonstrate that the carbon atoms in the aromatic ring are notably pronounced in HOMO-2, HOMO-3 as well.

It is established that the excited states at wavelength values of 263, 255 and 250 nm are due to the following electron density distributions HOMO \rightarrow LUMO, HOMO-1 \rightarrow LUMO and HOMO \rightarrow LUMO+1, respectively. Considering the above presented molecular orbitals contributions, we stated that these electronic transitions indicate an interaction between the hydrogen sulfate system and the pyridinium ring, i.e. $n \rightarrow \pi^*$ charge transfers. In light of this, the absorption bands at shorter wavelengths (245, 239 and 207 nm) are recognized as charge transfers HOMO-2 \rightarrow LUMO, HOMO-3 \rightarrow LUMO and HOMO-3 \rightarrow LUMO+1, respectively. These are denoted as electron density distribution in the aromatic ring of PHS, i.e. $\pi \rightarrow \pi^*$ charge transfers.

Figure 6 exposed that the absorption peaks in the UV-vis spectra of PHS/Al-NA and PHS/RHA samples are identical to those that characterize the electronic transitions in pure ionic liquid. In addition, the intensity of the bands of PHS/Al-NA and PHS/RHA is established to be remarkably higher in comparison with that of the bands registered for unsupported PHS. It suggests that a significant number of PHS sites available for an electron density distribution present on the Al-NA and RHA surfaces. It is interesting to point out that the absorption peaks of PHS/Al-NA are slightly more pronounced in intensity with respect to these of PHS/RHA, assuming that the PHS phase on the Al-NA surface should be in a more dispersed state than that on RHA. However, the XRD analysis clearly indicated that the PHS particles on Al-NA are significantly bigger in size than those on RHA. Moreover, the XPS showed that the silicon concentration on RHA surface decreases in a greater extent than aluminium one on Al-NA when they (supports) are impregnated with PHS. Hence, we believe that higher hindrance (expressed by a lower absorption) of the charge transfers in PHS/RHA sample in comparison with these in PHS/Al-NA is a consequence of a stronger IL-RHA surface interaction with respect to that between the ionic liquid and Al-NA carrier.

This statement is supported by a work of Jia et al. [76], where a UV-vis characterization of gold complexes with pyridine-based SNS ligands is presented. The authors reported that the absorption peaks at 225 and 321 nm in the pure pyridine-based SNS ligand become weaker when the gold complexes are produced, due to a charge transfer between the ligand and metal center.

3.4. Thermal properties

The TG and DSC curves for the thermal decomposition of Al-NA, RHA, PHS, PHS/Al-NA and PHS/RHA are shown in Fig. 7. As can be seen, the decomposition process of Al-NA support includes three thermal intervals, up to 110°C, from 140 to 280°C and 310-560°C. As it was already presented by XRD, phases of corundum, ammonium alunite and loncreeckite present in the Al-NA structure. Taking into account that a thermal decomposition of α -Al₂O₃ phase should not be expected, the observed temperature intervals are connected with degradation of ammonium alum.

Results showed that the mass loss in the first temperature region is 6.37%. Thereafter, a weight loss of 3.49% is detected in the temperature interval from 140-280°C. In addition, a values of 3.67% characterize the sample mass decreasing between 310-560°C. The DSC curve of Al-NA sample demonstrated the presence of three endothermic peaks – a strong one at 84°C and two low-intensive ones at 227 and 503°C. The first temperature region is due to removal of physisorbed water on the Al-NA surface and NH₄Al(SO₄)₂·12H₂O dehydration to NH₄Al(SO₄)₂ [77]. In the temperature interval from 140-280°C, NH₄Al(SO₄)₂ undergoes dehydroxylation and deammoniation ($2\text{NH}_4\text{Al}(\text{SO}_4)_2 \rightarrow \text{Al}_2(\text{SO}_4)_3 + 2\text{NH}_3 + \text{SO}_3 + \text{H}_2\text{O}$), while the sample mass decreasing between 310-560°C is related to desulphation of Al₂(SO₄)₃ to 3SO₃ and Al₂O₃.

The TG profile of pure RHA revealed a decomposition process before 200°C, accompanied by a minimal weight loss of 2.34%. Theafter, a monotonically mass loss decreasing (3.05%) up to 690°C is registered. Similar to Al-NA sample, the recorded weight loss in the first temperature region is due elimination of adsorbed water. Comparing the first decomposition peaks for pure Al-NA and RHA supports, it can be seen that the adsorbed water on the Al-NA is in a greater amount. The latter was undoubtedly confirmed by means of the corresponding DSC peaks. It is interesting to point out that a broad endothermic peak is observed in the temperature interval from 560 to 690°C. To explain this peak, the RHA content is taking into account. Considering that SiO₂ and CaCO₃ present

as phases in RHA (see XRD, XPS and FT-IR analyses), calcite is expected to decompose in some extent during a thermal treatment of RHA. Consequently, the observed weight loss of 3.05% in the current work is attributed to carbonates decomposition [78].

The PHS thermal behaviour showed decomposition steps in the intervals from 90 to 180°C and from 250 to 550°C (Fig. 7). While a value of 5.77% registered as a mass loss in the first temperature region, the weight decreases fast with elevating the temperature up to 550°C. At that temperature (550°C) the sample is completely decomposed with a total mass loss of 95.03%. The DSC curve of pure PHS clearly indicates two endothermic peaks, a broad one from 50 to 170°C and a very strong one centered at 390°C. In addition, an exothermic peak of low intensity is observed at 564°C. It is interesting to point out that the first endothermic peak starts from temperature of 50°C, which is notably lower than the temperature (90°C) characterizing the initial mass loss. In other words, an endothermic effect without a mass loss is detected. We believe that the endothermic effect within 50-90°C is a consequence of PHS melting [79]. The weight loss between 90 and 180°C is assigned to elimination of physisorbed water and/or carbonates, being already detected by FT-IR analysis (Fig. 5). Comparing the mass loss due to removal of physisorbed water from the Al-NA, RHA and PHS surfaces, it can be seen that adsorbed water amount decreases in the order Al-NA > PHS > RHA.

As it was noted above, the temperature within 250-550°C (expressed by an endothermic peak at 390°C) characterizes the complete PHS decay. To offer a plausible mechanism of PHS decomposition, the chemical bonds involved in the PHS structure are considered (see Fig. 2S). Previous our studies showed that the PHS formation includes an interaction between the fragments $[\text{HSO}_4]^-$ and $[\text{H-Pyr}]^+$ via $\text{S}^1-\text{O}^3\cdots\text{H}^7-\text{N}^{13}$ and $\text{S}^1-\text{O}^4\cdots\text{H}^{18}-\text{C}^{12}$ hydrogen bonds [80]. It was established that these bonds are electrostatic in nature, being observed in a greater extent for $\text{S}^1-\text{O}^4\cdots\text{H}^{18}-\text{C}^{12}$. Taking into account that the electrostatic bonds are weaker than those with a covalent nature [81], we suggested that a cleavage of the bonds $\text{S}^1-\text{O}^3\cdots\text{H}^7-\text{N}^{13}$ and $\text{S}^1-\text{O}^4\cdots\text{H}^{18}-\text{C}^{12}$ is the initial step of PHS degradation. As a result, pyridine and sulfuric acid fragments are formed. It is widely presented that the pyridine thermal decomposition proceeds at temperatures above 700°C, where H_2 , $\text{HC}\equiv\text{CH}$ and HCN are the major products [82]. Since the thermal analysis in the current work is in the temperature interval 30-700°C (*see pt. 2.2.*), the mass decreasing above 250°C should not be associated with a cleavage of C=C and/or N=C bonds in the aromatic ring. On the other hand, a value of 115°C is registered as a boiling point of pyridine [83]. Hence, it could be proposed that the pyridine (44.64% from the total mass of

PHS) formed above 250°C ($[\text{H-Pyr}]^+ [\text{HSO}_4]^- \rightarrow \text{Pyr} + \text{H}_2\text{SO}_4$) undergo a rapid evaporation. It causes the sample mass to decrease notably. Unlike pyridine, when sulfuric acid is above 300°C, it gradually decomposes to SO_3 and H_2O [83]. Thereafter, the sulfur trioxide is transformed into SO_2 and 0.5O_2 . We can summarize that the temperature interval between 250 and 550°C with the corresponding DSC peak express a PHS degradation to pyridine, SO_3 (or SO_2 and 0.5O_2) and H_2O . The exothermic peak detected at 564°C implies that some oxidation process has occurred, most likely with the participation of SO_3 and/or O_2 .

Analyzing the thermogram of PHS/Al-NA, four temperature regions of mass loss are detected – from 40 to 90°C (mass loss of 2.96%), between 120 and 200°C (mass loss of 3.75%), within 210-320°C (mass loss of 4.25%) and from 350 to 570°C (mass loss of 6.51%). The corresponding DSC peaks are centered at 80, 175, 260 and 530°C, respectively (Fig. 7). Comparing the TG profiles of pure Al-NA and PHS/Al-NA in the temperature interval up to 100°C, it can be observed that PHS/Al-NA sample is characterized with a lower mass loss. It is related to (i) a decreasing of exposed Al-NA surface during the ionic liquid deposition, as it was noted earlier by C 1s, Al 2p and S 2p core-electron levels and (ii) transformation of ammonium alum in $(\text{NH}_4)_2\text{S}_2\text{O}_5$ and $\text{Al}_2(\text{SO}_4)_3$. In addition, the O 1s analysis indicated that the peak at BE value of 533.2 eV (referred as adsorbed O-H groups) in the XPS spectrum of Al-NA cannot be found in the O 1s line of PHS/Al-NA sample. On the other hand, the same temperature region (up to 100°C) showed a lower mass loss of PHS/Al-NA (2.96%) in comparison with that of pure PHS (5.77%). This is due to formation of large in size PHS species on the Al-NA surface, being detected by XRD.

The mass loss between 120 and 200°C in the TG curve of PHS/Al-NA is associated with a decomposition of the immobilized ionic liquid. Obviously, the PHS degradation in PHS/Al-NA sample starts at a notably lower temperature with respect to that registered for pure PHS (above 250°C). Nevertheless, the mass loss for PHS/Al-NA (3.75%) in comparison with that for pure IL (95.03%) is found to be remarkably lower. The first effect is attributed to a surface IL-support interaction, which causes the impregnated PHS to decomposes earlier than pure ionic liquid. However, the PHS on the Al-NA surface is in the form of agglomerated particles, being observed by XRD. It implies that these will be hardly decomposed. The latter is confirmed in some extent, comparing the DSC profiles of PHS and PHS/Al-NA. Thus, the DSC curve of pure PHS described above clearly showed an exothermic peak, denoted as an oxidation process with the contribution of SO_3 and/or O_2 . However, no such exothermic peak is observed in the DSC profile of PHS/Al-NA. It suggests that notably low amounts of SO_3 are formed due to a hard decomposition behaviour of PHS

when it is deposited on Al-NA. The last two degradation steps (within 210-320°C and from 350 to 570°C) in the TG profile of PHS/Al-NA correspond to those observed above in the case of pure Al-NA support, namely deammoniation and desulphation, respectively. It should be noted that the mass loss (4.25%) due to PHS/Al-NA deammoniation is more pronounced than that registered in the case of Al-NA (3.53%). This is connected with an increased amount of NH_4^+ (revealed by N 1s and FT-IR studies) on the Al-NA support surface during the impregnation. The same tendency is also observed for the desulphation process. Hence, the mass loss (6.51%) due to PHS/Al-NA desulphation is established to be higher than that registered for Al-NA (3.67%). It is ascribed to additional sulphate groups present on the PHS/Al-NA surface (except those from support) in the form of $[\text{HSO}_4]^-$ fragments.

The TG curve of RHA supported pyridinium hydrogen sulfate showed two well-defined decomposition steps (Fig. 7). The first one is in the temperature interval 40-150°C, where a value of 8.53% is detected as a mass loss. The main decomposition step, expressed by a weight loss of 29.96%, is between 180 to 430°C. In this regard, two endothermic peaks, centered at 90 and 385°C, respectively, are observed in the DSC profile of PHS/RHA sample. The mass loss within 40-150°C (related to elimination of adsorbed water) revealed that the adsorbed water amount on the PHS/RHA surface is about 1.5 times higher than that on PHS (5.77%) and more than 3.5 times higher than that on RHA (2.34%). XRD analysis revealed that PHS particles cannot be detected on the RHA surface. On the other hand, the XPS study (C 1s, Si 2p and S 2p) showed that the exposed RHA surface decreases after PHS deposition. Hence, the above presented results are connected with highly dispersed PHS species present on the RHA surface, which leads to a higher adsorption capacity PHS/RHA with respect to that of pure PHS and RHA. The temperature interval from 180 to 430°C in the TG curve of PHS/RHA expresses a thermal degradation of the immobilized ionic liquid. It is interesting to point out that the PHS decomposition is characterized with an endothermic peak centered at a position (385°C), which is identical to that (390°C) detected earlier in the DSC profile of pure PHS. However, the mass loss in the case of PHS/RHA sample (29.96%) is established to be considerably lower than that detected for PHS (95.03%). These findings are correlated with a surface IL-RHA interaction, which prevents the PHS thermal decomposition in some extent.

Based on the XRD, XPS, FT-IR and UV-vis, it was established that the IL-RHA surface interaction is stronger than that between PHS and Al-NA support. As a result, the PHS phase on the Al-NA surface starts to decompose at lower temperatures than the PHS phase deposited on RHA. However, the highly dispersed PHS species formed on the RHA surface (due to

strong IL-RHA interaction) undergo a thermal decomposition in a greater extent (expressed by mass loss of 29.96%) in comparison with larger ones on the Al-NA surface, where a mass loss of 3.75% due PHS degradation is detected.

3.5. Catalytic activity

The catalytic performance of the obtained PHS/Al-NA and PHS/RHA samples is evaluated by a process of acetic acid esterification with 1-butanol at reaction temperature of 80°C, initial alcohol-to-acid molar ratio of unit and catalyst loading of 10 wt.% (Fig. 8). For comparison, the substrate (acetic acid) conversion for non-catalyzed (blank) reaction is presented as well. It is established that a value of 0.049 characterizes the acetic acid conversion when the esterification process is conducted without a catalyst. However, the addition of PHS/Al-NA and PHS/RHA (10 wt.%) considerably increased the substrate conversion up to 0.278 and 0.512, respectively. Comparing the substrate conversion in the presence of PHS/RHA and PHS/Al-NA, it is clear that the catalytic performance of the former one in the butyl acetate synthesis is more pronounced than that of the Al-NA supported IL. This is trying to be explain as follows.

It is well known that the activation of a carboxylic acid in the presence of a Brønsted acidic ionic liquid proceeds via proton transfer (formation of a hydrogen bond) from the IL particles towards the substrate [84]. As a result, an active complex due to a carboxylic acid-catalyst interaction is obtained. In this sense, it could be stated that a greater number of IL particles present on the support surface will lead to a formation of a greater number of active complexes. XRD, FT-IR, XPS and UV-vis analyses in the current work clearly indicated a stronger IL-RHA surface interaction than that between PHS and Al-NA. As a result, the PHS phase on the RHA surface is established to be remarkably more dispersed in comparison with that on the Al-NA. Based on this, more prominent activity of the PHS/RHA catalyst (with respect to that of PHS/Al-NA) in the process of acetic acid esterification with butanol is related to the presence of a great number of active sites on the RHA surface, available for substrate activation. Considering that the ionic liquids are materials with a relatively high viscosity, PHS particles with a large size on the Al-NA surface (a consequence of a weak surface IL-support interaction) imply a slow mass transfer of the substrate into the active phase (PHS). In other words, a great part of a given ionic liquid catalyst droplet will not be in contact with the substrate. The latter limits the overall reaction rate and reduces the ion-

ic liquid contribution in the reaction. A plausible reaction mechanism for butyl acetate synthesis in the presence of PHS/Al-NA and PHS/RHA catalysts is illustrated in Fig. 9.

4. Conclusions

Electronic, thermal and catalytic behavior of rice husk ash (RHA) and corundum (Al-NA) supported pyridinium hydrogen sulfate (PHS) as a function of the interphase interactions was studied. Characterization methods such as N_2 adsorption-desorption measurements, XRD, FT-IR, XPS, UV-*vis*, and TG/DSC were applied for investigation the surface features in the synthesized catalysts (PHS/RHA and PHS/Al-NA). The catalytic activity of PHS/RHA and PHS/Al-NA was considered in a process of butyl acetate synthesis.

The N_2 adsorption-desorption measurements showed that the obtained catalysts are mesoporous materials with a pore diameter between 10 and 30 nm. However, a contribution of micropores was observed as well. XRD analysis established that a PHS particles with an average size of 31.5 nm present on the Al-NA support surface when PHS/Al-NA is obtained.

In contrast, diffraction peaks due to PHS particles on the RHA surface were not detected, which allowed us to state that these are highly dispersed. We attributed these effects to a stronger surface PHS-RHA interaction than that between PHS and Al-NA. The latter was confirmed by UV-*vis* study, where the electronic transition in PHS/RHA are observed to be more hindered than those in the case of PHS/Al-NA. Based on the FT-IR and XPS analyses, we proposed that the aforementioned surface interactions are in the form of $Al(Si)-O\cdots H-N$ and $Al(Si)-O-S$ bonds between the metal cations (Al^{3+} and Si^{4+}) in the carriers and the fragments ($[H-Pyr]^+$ and $[HSO_4]^-$) in the PHS. Stronger IL-RHA interaction caused the PHS phase deposited on RHA to decompose at higher temperature ($180^\circ C$) than that ($120^\circ C$) required for PHS degradation on Al-NA. However, agglomerated PHS species on Al-NA surface were decomposed in a lesser extent (mass loss of 3.75%) in comparison with more dispersed ones on RHA, where a mass loss of 29.96% was recorded. The catalytic test established a more prominent catalytic activity of PHS/RHA with respect to that of PHS/Al-NA in the process of butyl acetate synthesis. It was related to a great number of active sites present on the RHA surface (due to a stronger PHS-RHA interaction), available for substrate activation. Larger PHS particles on the Al-NA surface implied that a great part of a given ionic liquid droplet will not be in a contact with the substrate, which limits the over-

all reaction rate. A plausible reaction mechanism for butyl acetate synthesis illustrated in Fig. 9.

References

- [1] H. Li, P. S. Bhadury, B. Song, S. Yang, Immobilized functional ionic liquids: Efficient, green, and reusable catalysts, *RSC Adv.* 2 (2012) 12525-12551.
- [2] I. Tankov, R. Yankova, DFT analysis, reaction kinetics and mechanism of esterification using pyridinium nitrate as a green catalyst, *J. Mol. Liq.* 277 (2019) 241–253.
- [3] D. J. Tao, X. M. Lu, J. F. Lu, K. Huang, Z. Zhou, Y. T. Wu, Noncorrosive ionic liquids composed of [HSO₄] as esterification catalysts, *Chem. Eng. J.* 171 (3) (2011) 1333-1339.
- [4] Y. Tao, R. Dong, I. V. Pavlidis, B. Chen, T. Tan, Using imidazolium-based ionic liquids as dual solvent-catalysts for sustainable synthesis of vitamin esters: Inspiration from bio- and organo-catalysis, *Green Chem.* 18 (2016) 1240–1248.
- [5] H. Amirfirouzkouhi, A.N. Kharat, Application of ionic liquids as recyclable green catalysts for selective alkylation of phenol, *Sep. Purif. Technol.* 196 (2018) 132-139.
- [6] B. V. Romanovsky, I.G. Tarkhanova, Supported ionic liquids in catalysis, *Russ. Chem. Rev.* 86 (2017) 444–458.
- [7] A. Riisager, B. Jørgensen, P. Wasserscheid, R. Fehrmann, First application of supported ionic liquid phase (SILP) catalysis for continuous methanol carbonylation, *Chem. Commun.* 9 (2006) 994-996.
- [8] M. H. Valkenberg, C. de Castro, W. F. Hölderich, Immobilisation of chloroaluminate ionic liquids on silica materials, *Top. Catal.* 14 (2001) 139–144.
- [9] J. M. Anderson, A. Baiker, Interactions of 1-ethyl-3-methylimidazolium trifluoromethanesulfonate ionic liquid with alumina nanoparticles and organic solvents studied by infrared spectroscopy, *J. Phys. Chem. C* 117 (2013) 12210–12217.
- [10] Y. Wang, W. Lou, X. Wang, A green way to synthesize lubricating ester oils: The esterification of pentaerythritol with fatty acids at stoichiometric ratio over [BHSO₃MMIm]⁺[HSO₄]⁻/SiO₂, *Catal. Commun.* 111 (2018) 21–25.
- [11] Y. He, Q. Zhang, X. Zhan, D. guo Cheng, F. Chen, Synthesis of efficient SBA-15 immobilized ionic liquid catalyst and its performance for Friedel-Crafts reaction, *Catal. Today.* 276 (2016) 112–120.

- [12] M.J. Mohammed, K.M. Hello, A.M. Yasser, F. Adam, Z. Farag, Modification of silica rice husk ash to solid ammonium sulfate for second generation biofuels productions, *J. Catalyst* 2014 (2014) 128547.
- [13] F. Shirini, M. Seddighi, O. Goli-Jolodar, Facile and efficient synthesis of pyrimido[1,2-a]benzimidazole and tetrahydrobenzimidazo[2,1-b]quinazolin-1(2H)-one derivatives using Brønsted acidic ionic liquid supported on rice husk ash (RHA-[pmim]HSO₄), *J. Iran. Chem. Soc.* 13 (2016) 2013–2018.
- [14] D. A. Beattie, A. Arcifa, I. Delcheva, B.A. Le Cerf, S. V. MacWilliams, A. Rossi, M. Krawowska, Adsorption of ionic liquids onto silver studied by XPS, *Colloids Surfaces A Physicochem. Eng. Asp.* 544 (2018) 78–85.
- [15] J. Végh, The Shirley background revised, *J. Electron Spectrosc. Relat. Phenom.* 151 (3) (2006) 159-164.
- [16] J. H. Scofield, Hartree-Slater subshell photoionization cross-sections at 1254 and 1487 eV, *J. Electron Spectrosc. Relat. Phenom.* 8 (2) (1976) 129-137.
- [17] A. N. Saud, H. S. Majdi, S. N. Saud, Synthesis of nano-alumina powder via recrystallization of ammonium alum, *Cerâmica* 65 (2019) 236-239.
- [18] L. Li, M. Chen, Y. Dong, X. Dong, S. Cerneaux, S. Hampshire, J. Cao, L. Zhu, Z. Zhu, J. Liu, A low-cost alumina-mullite composite hollow fiber ceramic membrane fabricated via phase-inversion and sintering method, *J. Europ. Ceram. Soc.* 36 (2016) 2057–2066.
- [19] J. Lewis, D. Schwarzenbach, H. D. Flack, Electric field gradients and charge density in corundum, α -Al₂O₃, *Acta Cryst.* A38 (1982) 733-739.
- [20] S. Cava, S. M. Tebcherani, I. A. Souza, S. A. Pianaro, C. A. Paskocimas, E. Longo, J. A. Varela, Structural characterization of phase transition of Al₂O₃ nanopowders obtained by polymeric precursor method, *Mater. Chem. Phys.* 103 (2007) 394–399.
- [21] S. P. Altaner, J. J. Fitzpatrick, M. D. Krohn, P. M. Bethke, D. O. Hayba, J. A. Goss, Z. A. Brown, Ammonium in alunites, *Am. Mineral.* 73 (1988) 145-152.
- [22] A. Z. Molina, J. del Ángel Soto, M. M. Rosales, R. R. Toledo, Ammonium alunite and basic aluminum sulfate: effect of precipitant agent, *Int. J. Mater. Sci. Applic.* 4(2) (2015) 96-100.
- [23] C. M. A. McQueen, J. J. Łucejko, I. M. T. Flâte, F. Modugno, S. Braovac, Ammonium alum in alum-treated wooden artefacts: discovery, origins and consequences, *Herit. Sci.* 7 (2019) 78-89.

- [24] V. Žáček, R. Škoda, F. Laufek, F. Košek, J. Jehlička, Complementing knowledge about rare sulphates loncreekite, $\text{NH}_4\text{Fe}^{3+}(\text{SO}_4)_2 \cdot 12\text{H}_2\text{O}$ and sabeite, $\text{NH}_4\text{Fe}^{3+}(\text{SO}_4)_2$: chemical composition, XRD and RAMAN spectroscopy, *J. Geosci.* 64 (2019), 149–159.
- [25] R. D. Rogers, C. B. Bauer, Crystal structure of pyridinium hydrogen sulfate, $[\text{HC}_5\text{H}_5\text{N}][\text{HSO}_4]$, *J. Chem. Crystallogr.* 24 (1994) 285–287.
- [26] Y. Shen, C. Areeprasert, B. Prabowo, F. Takahashia, K. Yoshikawa, Metal nickel nanoparticles in situ generated in rice husk char for catalytic reformation of tar and syngas from biomass pyrolytic gasification, *RSC Adv.* 4 (2014) 40651–40664.
- [27] J. Harris, I. Mey, M. Hajir, M. Mondeshki, S. E. Wolf, Pseudomorphic transformation of amorphous calcium carbonate films follows spherulitic growth mechanisms and can give rise to crystal lattice tilting, *Cryst. Eng. Comm.* 17 (2015) 6831–6837.
- [28] M. Sobota, I. Nikiforidis, W. Hieringer, N. Paape, M. Happel, H.-P. Steinrück, A. Göring, P. Wasserscheid, M. Laurin, J. Libuda, Toward ionic-liquid-based model catalysis: growth, orientation, conformation, and interaction mechanism of the $[\text{Tf}_2\text{N}]^-$ anion in $[\text{BMIM}][\text{Tf}_2\text{N}]$ thin films on a well-ordered alumina surface, *Langmuir* 26 (10) (2010) 7199–7207.
- [29] M.J.F. Martins, A.R. Ferreira, E. Konstantinova, H.A. de Abreu, W.F. Souza, S.S.X. Chi-aro, L.G. Dias, A.A. Leitão, Interactions between 1-butyl-3-methylimidazolium tetrafluoroborate ionic liquid and $\gamma\text{-Al}_2\text{O}_3$ (100) surface calculated by density functional theory, *Int. J. Quantum Chem.* 112 (19) (2012) 3234–3239.
- [30] Y. Guo, G. Lu, Z. Zhang, L. Jiang, X. Wang, S. Li, B. Zhang, J. Niu, Effects of $\text{ZrO}_2/\text{Al}_2\text{O}_3$ properties on the catalytic activity of Pd catalysts for methane combustion and CO oxidation-Catal. Today 126 (2007) 441–448.
- [31] I. Tankov, R. Yankova, Quantum mechanical and reaction dynamics investigation of butyl acetate synthesis in the presence of pyridinium hydrogen sulfate, *J. Mol. Liq.* 278 (2019) 183–194.
- [32] C. Zhang, Z. Xu, Y. Hu, J. He, M. Tian, J. Zhou, Q. Zhou, S. Chen, D. Chen, P. Chen, W. Sun, Novel insights into the hydroxylation behaviors of $\alpha\text{-quartz}$ (101) surface and its effects on the adsorption of sodium oleate, *Minerals* 9 (2019) 450–469.
- [33] W. M. Haynes, (2016–2017). CRC Handbook of Chemistry and Physics, 97th Edition (CRC Handbook of Chemistry & Physics) 97th Edition. CRC Press. ISBN 978-1498754286.
- [34] M. Thommes, K. Kaneko, A. V. Neimark, J. P. Olivier, F. Rodriguez-Reinoso, J. Rouquerol, K. S. W. Sing, Physisorption of gases, with special reference to the evaluation of

surface area and pore size distribution (IUPAC Technical Report) *Pure Appl. Chem.* 87 (9-10) (2015) 1051–1069.

[35] T. Horikawa, D.D. Do, D. Nicholson, Capillary condensation of adsorbates in porous materials, *Adv. Colloid Interface Sci.* 169 (2011) 40–58.

[36] G. Leofanti, M. Padovan, G. Tozzola, B. Venturelli, Surface area and pore texture of catalysts, *Catal. Today* 41 (1998) 207-219.

[37] I. Tankov, R. Yankova, A combined DFT and FT-IR study on the surface interactions in alumina supported ionic liquid [H-Pyr]⁺[HSO₄]⁻, *Spectrochim. Acta Part A: Mol. Biomol. Spectrosc.* 226 (2020) 117545.

[38] H. Sarvamangala, V. B. Raghavendra, S. T. Girisha, Biobenefication of oxide minerals from bacillus subtilis using FTIR and MALDI-TOF techniques, *J. Environm. Protect.* 8 (2017) 194-205.

[39] A. Boumaza, A. Djelloul, F. Guerrab, Specific signatures of α -alumina powders prepared by calcination of boehmite or gibbsite, *Powder Technol.* 201 (2010) 177–180.

[40] R. Tayebee, M. Jomei, B. Maleki, M. K. Razi, H. Veisi, M. Bakherad, A new natural based ionic liquid 3-sulfonic acid 1-imidazolopyridinium hydrogen sulfate as an efficient catalyst for the preparation of 2H-indazolo[2,1-b]-phthalazine-1,6,11(13H)-triones, *J. Mol. Liq.* 206 (2015) 119–128.

[41] F.J. Gracia, S. Guerrero, E.E. Wolf, J.T. Miller, A.J. Kropf, Kinetics, operando FTIR, and controlled atmosphere EXAFS study of the effect of sulfur on Pt-supported catalysts during CO oxidation, *J. Catal.* 233 (2005) 372-387.

[42] A. R. Kampf, R. P. Richards, B. P. Nash, J. B. Murowchick, J. F. Rakovan, Carlsonite, (NH₄)₅Fe₃³⁺O(SO₄)₆·7H₂O, and huizingite-(Al), (NH₄)₉Al₃(SO₄)₈(OH)₂·4H₂O, two new minerals from a natural fire in an oil-bearing shale near Milan, Ohio, *Am. Min.* 101 (2016) 2095–2107.

[43] J. Safari, Z. Zarnegar, Brønsted acidic ionic liquid based magnetic nanoparticles: a new promoter for the Biginelli synthesis of 3,4-dihydropyrimidin-2(1H)-ones/thiones, *New J. Chem.* 38 (2014) 358-365.

[44] G. Zu, J. Shen, X. Wei, X. Ni, Z. Zhang, J. Wang, G. Liu, Preparation and characterization of monolithic alumina aerogels, *J. Non-Cryst. Solids* 357 (2011) 2903-2906.

[45] W. Pongdong, C. Nakason, C. Kummerlöwe, N. Vennemann, Influence of filler from a renewable resource and silane coupling agent on the properties of epoxidized natural rubber vulcanizates, *J. Chem.* 2015 (2015) 796459.

- [46] S. Gunasekaran, G. Anbalagan, S. Pandi, Raman and infrared spectra of carbonates of calcite structure, *J. Raman Spectrosc.* 37 (2006) 892–899.
- [47] D. Carboni, B. Lasio, V. Alzari, A. Mariani, D. Loche, M. F. Casula, L. Malfattia, P. Innocenzi, Graphene-mediated surface enhanced Raman scattering in silica mesoporous nanocomposite films, *Phys. Chem. Chem. Phys.* 16 (2014) 25809-25818.
- [48] A. Periasamy, S. Muruganand, M. Palaniswamy, Vibrational studies of Na_2SO_4 , K_2SO_4 , Na-HSO_4 and KHSO_4 crystals, *Rasayan J. Chem.* 2 (4) (2009) 981-989.
- [49] D. Gandolfo, J. Zarembowitch, Apport de la coordination des heterocycles a la connaissance de leurs spectres infrarouge et Raman. III-Spectres de la methyl-3 pyridine *Spectrochim, Acta* 33 (1977) 615-623.
- [50] Y. Zhang, H. He, S. Zhang, M. Fan, Hydrogen-bonding interactions in pyridinium-based ion-ic liquids and dimethyl sulfoxide binary systems: a combined experimental and computational study, *ACS Omega* 3 (2018) 1823-1833.
- [51] B. C. Adhikari, J. S. Kim, S. Mumtaz, R. Paneru, P. Lamichhane, B. K. Min, J. H. Jang, E. H. Choi, Effective radius of adatoms/single atom of polycrystalline W nanotip in gas field ion source, *Curr. Appl. Phys.* 20 (5) (2020) 707-714.
- [52] B. C. Smith, The C-O Bond, Part I: Introduction and the infrared spectroscopy of alcohols, *Spectrosc.* 32 (1) (2017) 14-21.
- [53] L. V. Duong, B. J. Wood, J. T. Kloprogge, XPS study of basic aluminum sulphate and basic aluminium nitrate, *Mater. Lett.* 59 (2005) 1932–1936.
- [54] Z. D. Hood, S. P. Adhikari, S. F. Evans, H. Wang, Y. Li, A. K. Naskar, M. Chi, A. Lachgar, M. P. Paranthaman, Tire-derived carbon for catalytic preparation of biofuels from feedstocks containing free fatty acids, *Carbon Resour. Convers.* 1 (2) (2018) 165-173.
- [55] K. Kai, W. Yingbin, Effect of aluminum phase in the formation process of thaumasite, *Ma-ter. Res. Innov.* 23 (6) (2019) 369-374.
- [56] H. Khan, I. K. Swati, M. Younas, A. Ullah, Chelated nitrogen-sulphur-codoped TiO_2 : synthesis, characterization, mechanistic, and UV/Visible photocatalytic studies, *Int. J. Photoenerg.* 2017 (2017) 7268641.
- [57] S. Dahle, F. Voigts, W. Maus-Friedrichs, In situ preparation of calcium carbonate films, *Thin Solid Films* 520 (2012) 1842–1846.
- [58] P. Post, L. Wurlitzer, W. Maus-Friedrichs, A. P. Weber, Characterization and applications of nanoparticles modified in-flight with silica or silica-organic coatings, *Nanomater.* 8 (7) (2018) E530.

- [59] M. Ni, B. D. Ratner, Differentiating calcium carbonate polymorphs by surface analysis techniques – an XPS and TOF-SIMS study, *Surf. Interface Anal.* 40 (2008) 1356–1361.
- [60] Z. Cao, A. Duan, Z. Zhao, J. Li, Y. Wei, G. Jiang, J. Liu, A simple two-step method to synthesize the well-ordered mesoporous composite Ti-FDU-12 and its application in the hydrodesulfurization of DBT and 4,6-DMDBT, *J. Mater. Chem. A* 2 (2014) 19738-19749.
- [61] P. M. K. Reddy, S. Mahammadunnisa, B. Ramaraju, B. Sreedhar, C. Subrahmanyam, Low-cost adsorbents from bio-waste for the removal of dyes from aqueous solution, *Environ. Sci. Pollut. Res.* 20 (6) (2013) 4111-4124.
- [62] M. Watanabe, H. Ando, T. Handa, T. Ichino, N. Kuwaki, Comparative XPS study of silver and copper surfaces exposed to flowing air containing low concentration of sulfur dioxide, *Zairyo-to-Kankyo* 56 (2007) 10-15.
- [63] C. Petit, M. Seredych, T. J. Bandoz, Revisiting the chemistry of graphite oxides and its effect on ammonia adsorption, *J. Mater. Chem.* 19 (2009) 9176–9185.
- [64] T. L. Barr, S. Seal, K. Wozniak, J. Klinowski, ESCA studies of the coordination state of aluminium in oxide environments, *J. Chem. Soc. Faraday Trans.* 93 (1997) 181-186.
- [65] A. Thøgersen, J. H. Selj, E. S. Marstein, Oxidation effects on graded porous silicon anti-reflection coatings, *J. Electrochem. Soc.* 159 (5) 2012) 276-281.
- [66] J. Shah, M. Ranjan, V. Davariya, S. K. Gupta, Y. Sonvane, Temperature-dependent thermal conductivity and viscosity of synthesized α -alumina nanofluids, *Appl Nanosci.* 7 (2017) 803–813.
- [67] J. F. McIntyre, R. T. Foley, B. F. Brown, Ultraviolet spectra of aluminum salt solutions, *Inorg. Chem.* 21 (1982) 1167-1172
- [68] M. K. Trivedi, A. Branton, D. Trivedi, G. Nayak, K. Bairwa, S. Jana, Fourier transform infra-red and ultraviolet-visible spectroscopic characterization of ammonium acetate and ammonium chloride: an impact of biofield treatment, *Mod. Chem. Appl.* 3 (3) (2015) 1000163.
- [69] M. H. Kim, D. Lee, H.-Y. Woo, T.-H. Kim, T. Paik, K.-S. Kim, Synthesis of colloidal aluminum hydroxide nanoparticles for transparent luminescent polymer nanocomposite films, *Ma-ter. Des.* 175 (2019) 107800.
- [70] S. Sun, H. Ding, X. Hou, Preparation of $\text{CaCO}_3\text{-TiO}_2$ composite particles and their pigment properties, *Mater.* 11(7) (2018) 1131-1142.
- [71] S. Venkateswaran, R. Yuvakkumar, V. Rajendran, Nano silicon from nano silica using natural resource (RHA) for solar cell fabrication, *Phosphorus Sulfur Silicon* 188 (2013) 1178–1193.

- [72] E.U. Gross, W. Kohn, Time-dependent density-functional theory, *Adv. Quantum Chem.* 21 (1990) 255-291.
- [73] N. M. O'Boyle, A. L. Tenderholt, K. M. Langner, cclib, A library for package-independent computational chemistry algorithms, *J. Comput. Chem.* 29 (5) (2008) 839-845.
- [74] C. S. Hansen, Ultraviolet photodissociation of protonated pyridine derivatives: action spectroscopy and mass spectrometry, Doctor of Philosophy thesis, School of Chemistry, University of Wollongong, 2016.
- [75] O. N. E. H. Kaabeche, R. Zouaghi, S. Boukhedoua, S. Bendjabeur, T. Sehili, A comparative study on photocatalytic degradation of pyridinium – based ionic liquid by TiO₂ and ZnO in aqueous solution, *Int. J. Chem. React. Eng.* 17 (9) (2019) 0253.
- [76] W.-G. Jia, Y.-C. Dai, H.-N. Zhang, X. Lu, E.-H. Sheng, Synthesis and characterization of gold complexes with pyridine-based SNS ligands and as homogeneous catalysts for reduction of 4-nitrophenol, *RSC Adv.* 5 (2015) 29491–29496.
- [77] J. López-Beceiro, J. Pascual-Cosp, R. Artiaga, J. Tarrío-Saavedra, S. Naya, Thermal characterization of ammonium alum, *J. Therm. Anal. Calorim.* 104 (2011) 127–130.
- [78] I. J. Fernandes, F. A. L. Sánchez, J. R. Jurado, A. G. Kieling, T. L. A. C. Rocha, C. A. M. Moraes, V. C. Sousa, *Adv. Powd. Technol.* 28 (2017) 1228–1236.
- [79] I. Tankov, R. Yankova, M. Mitkova, Dicho Stratiev, Non-isothermal decomposition kinetics of pyridinium nitrate under nitrogen atmosphere, *Thermochim. Acta* 665 (2018) 85–91.
- [80] I. Tankov, R. Yankova, S. Genieva, M. Mitkova, D. Stratiev, Density functional theory study on the ionic liquid pyridinium hydrogen sulfate, *J. Mol. Struct.* 1139 (2017) 400-406.
- [81] I. Tankov, R. Yankova, Theoretical (density functional theory) studies on the structural, electronic and catalytic properties of the ionic liquid 4-amino-1H-1,2,4-triazolium nitrate, *J. Mol. Liq.* 269 (2018) 529–539.
- [82] Y. Ninomiya, Z. Dong, Y. Suzuki, J. Koketsu, Theoretical study on the thermal decomposition of pyridine, *Fuel* 79 (2000) 449–457.
- [83] W. M Haynes (2014). *CRC Handbook of Chemistry and Physics* (95 ed.). CRC Press. 4–92. ISBN 9781482208689.
- [84] R. Skoda-Földes, The use of supported acidic ionic liquids in organic synthesis, *Molecules* 19 (2014) 8840-8884.

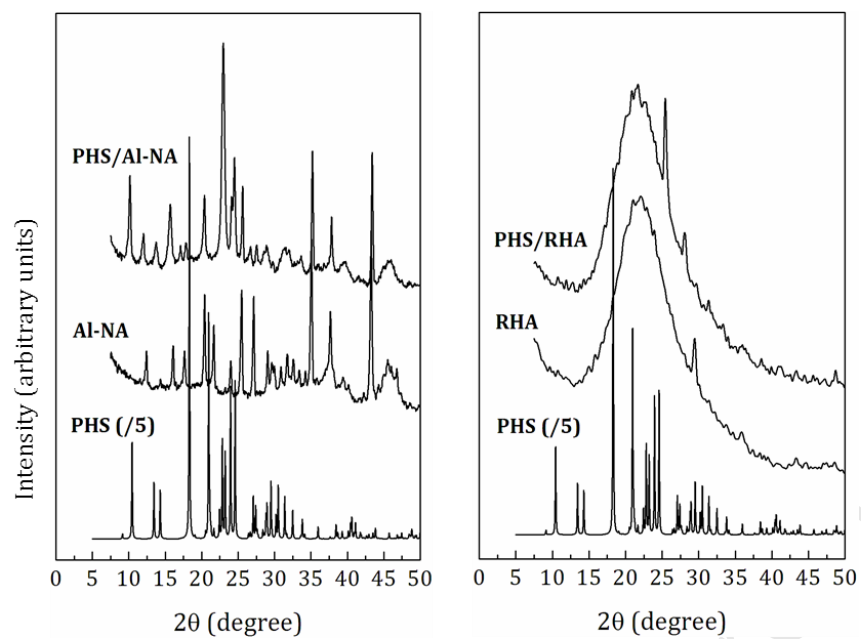


Fig. 1. X-ray diffractograms of Al-NA, RHA, PHS, PHS/Al-NA and PHS/RHA.

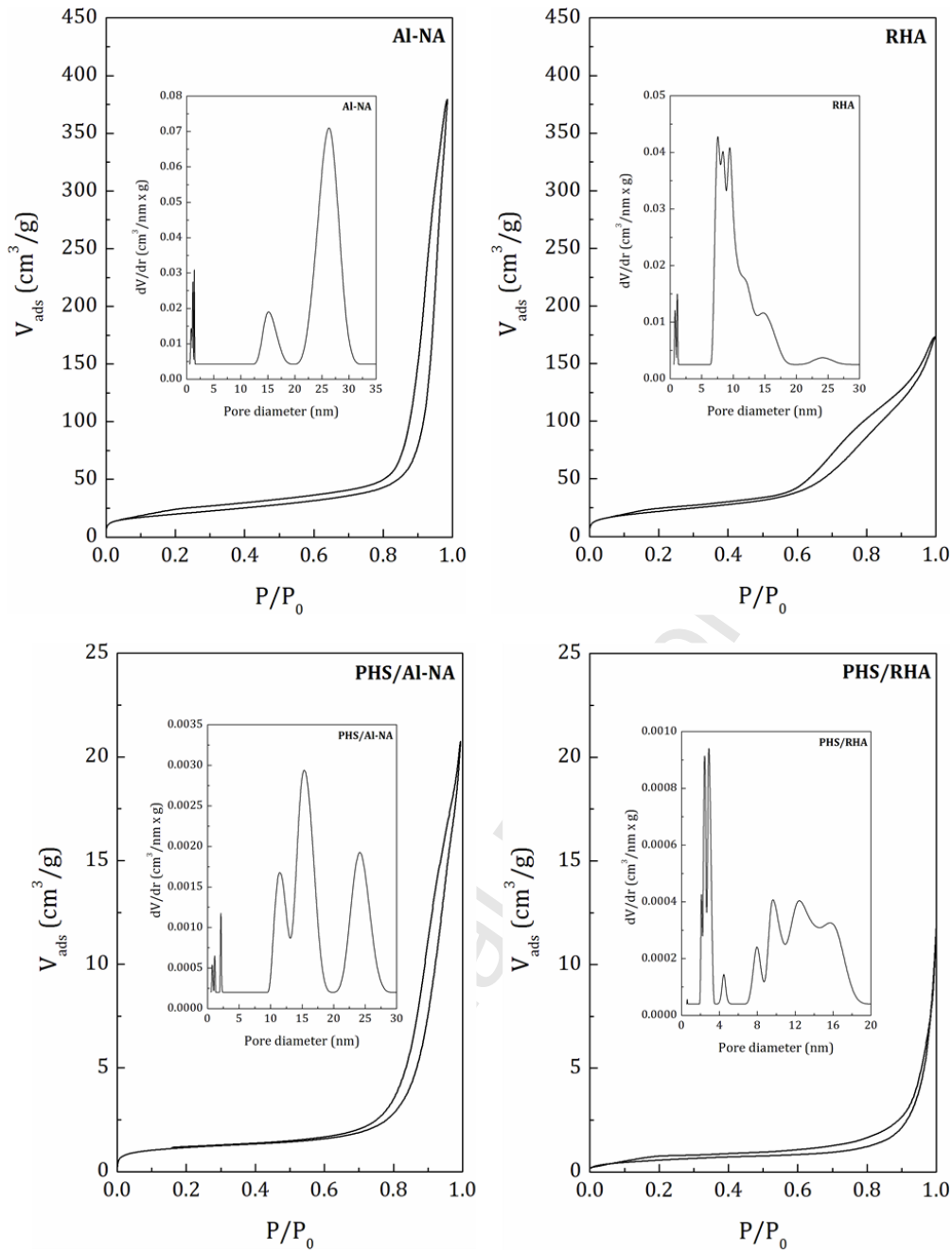


Fig. 2. N₂ adsorption-desorption isotherms and pore size distribution for Al-NA, RHA, PHS/RHA and PHS/Al-NA.

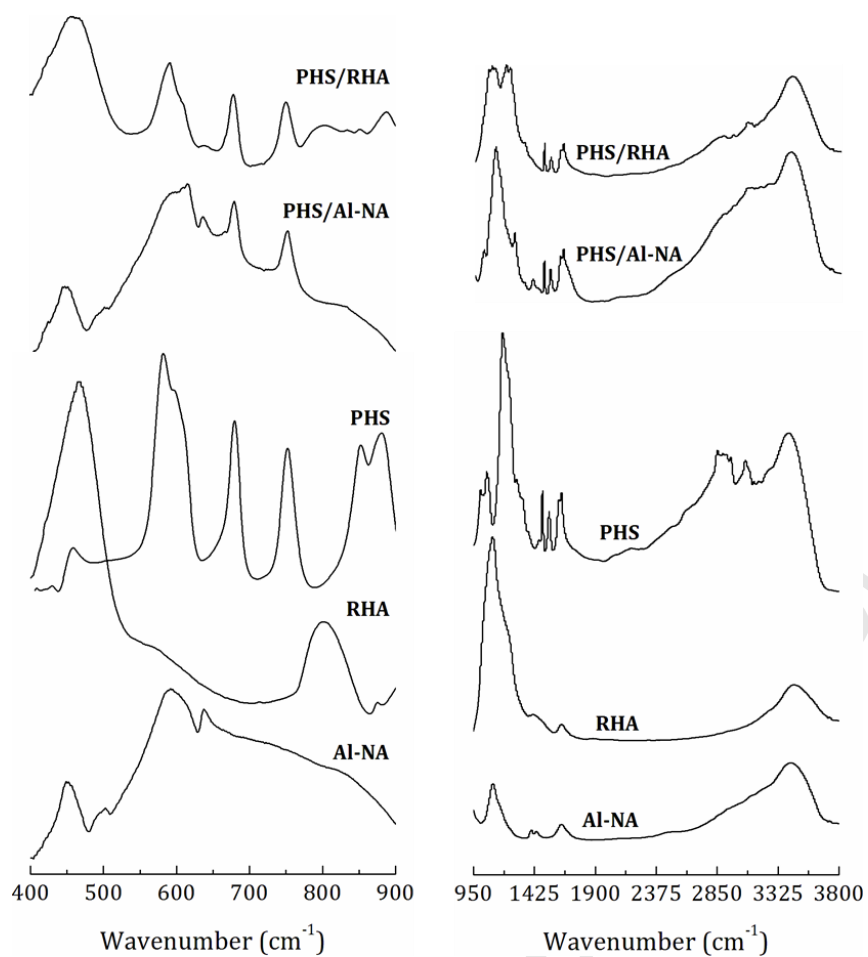


Fig. 3. FT-IR spectra of Al-NA, RHA, PHS, PHS/Al-NA and PHS/RHA in the regions from 400 to 900 cm^{-1} and from 950 to 3800 cm^{-1} .

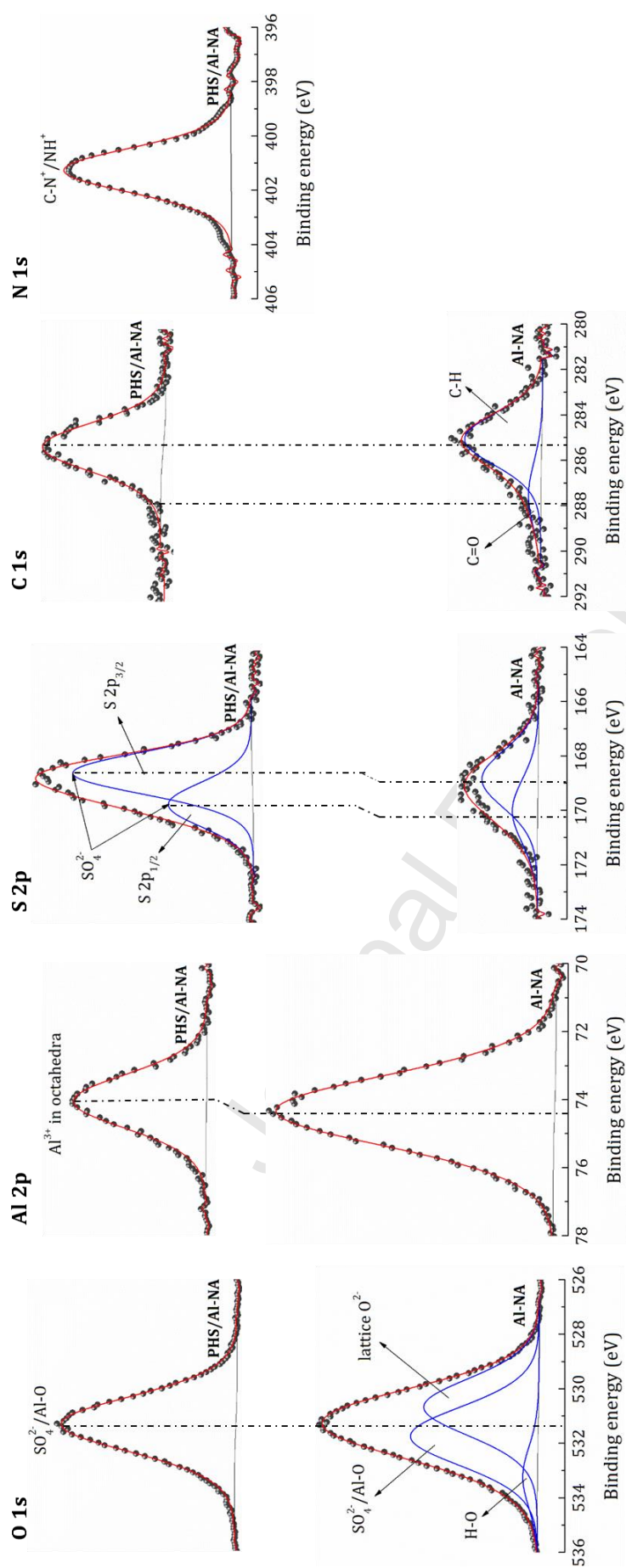


Fig. 4. XPS core electron levels in Al-NA and PHS/Al-NA.

Journal Pre-proof

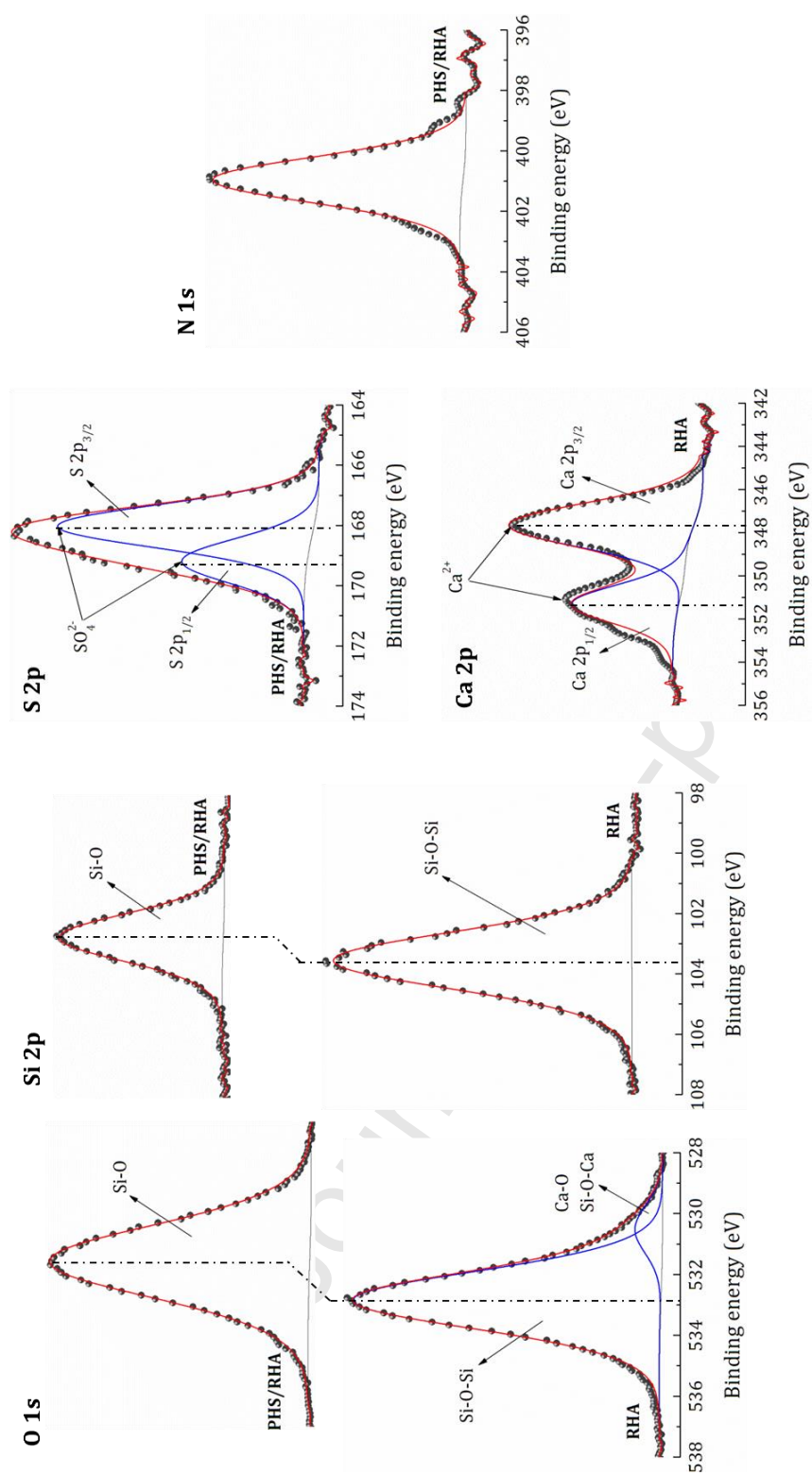


Fig. 5. XPS core electron levels in RHA and PHS/RHA.

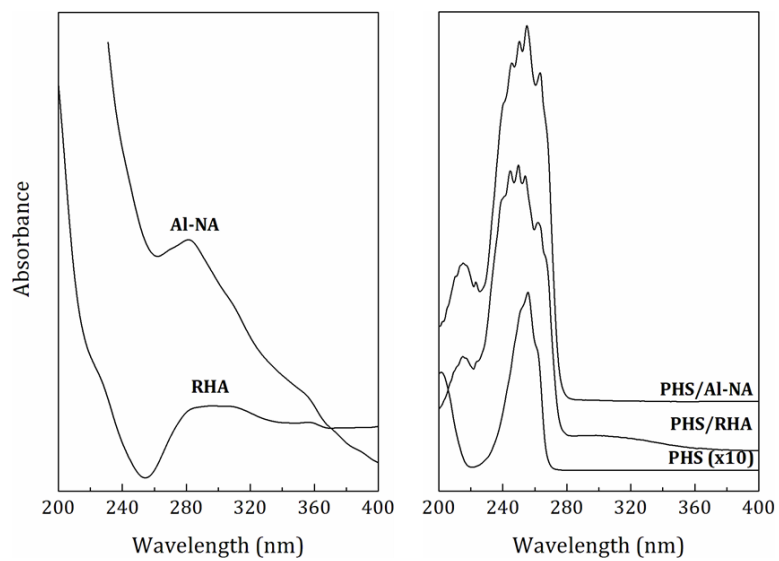


Fig. 6. Electronic absorption spectra of RHA, Al-NA, PHS, PHS/RHA and PHS/Al-NA.

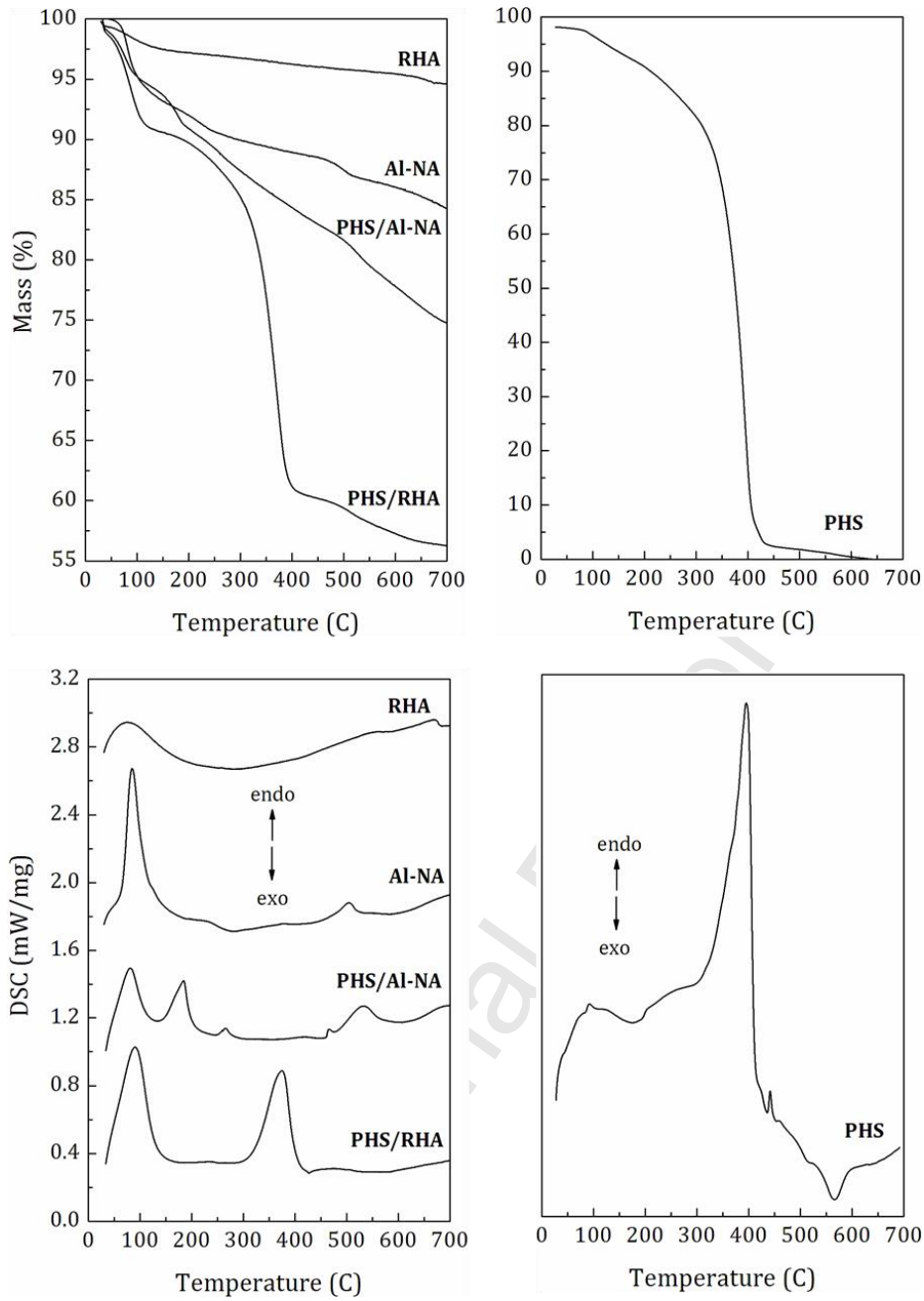


Fig. 7. TGA and DSC curves for thermal decomposition of Al-NA, RHA, PHS, PHS/Al-NA and PHS/RHA.

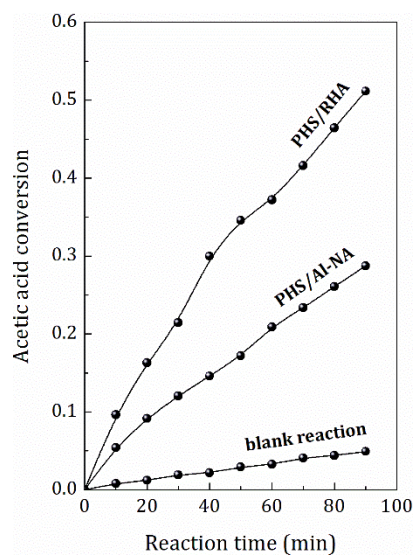


Fig. 8. Acetic acid conversion as a function of the catalyst nature.

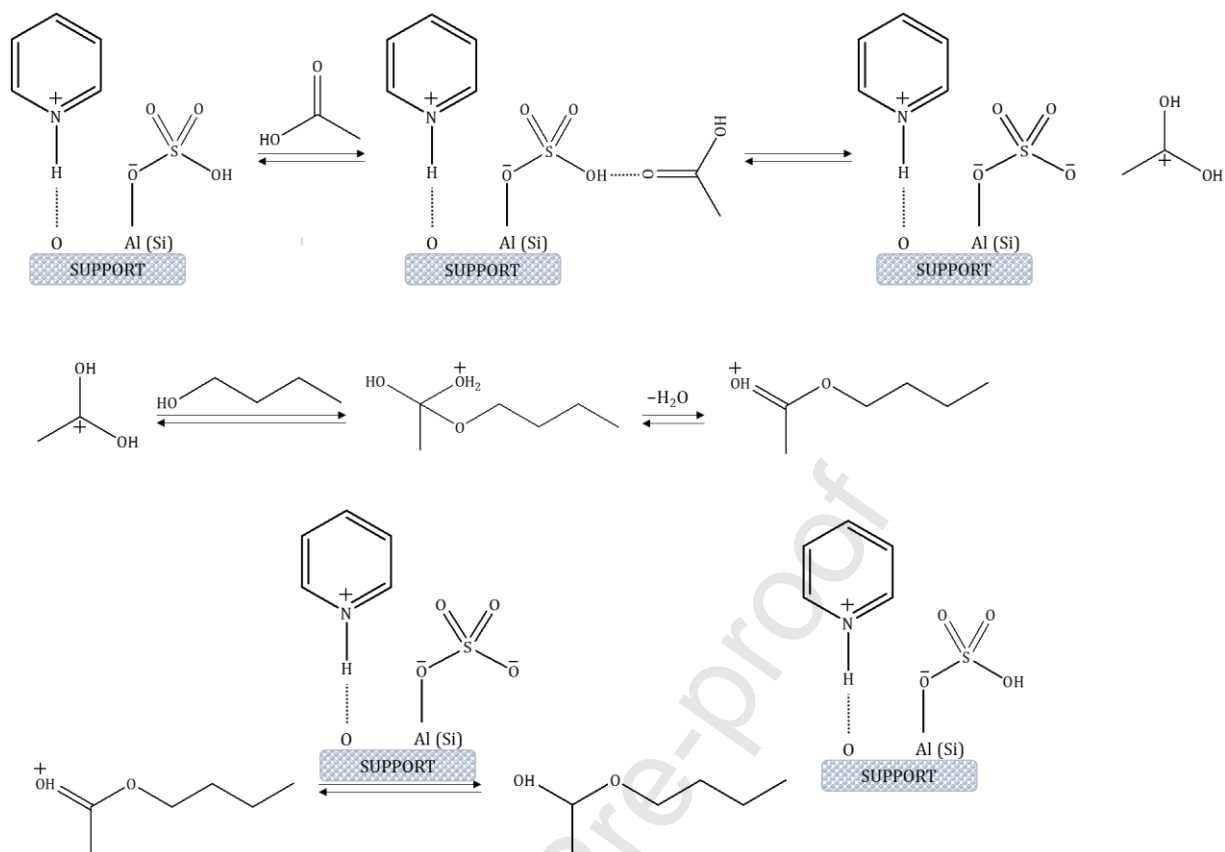


Fig. 9. A plausible reaction mechanism for butyl acetate synthesis in the presence of PHS/Al-NA and PHS/RHA catalysts.

Table 1. Textural properties of the investigated samples.

Sample	$S_{\text{BET}}, \text{m}^2/\text{g}$	$V_{\text{total}}, \text{cm}^3/\text{g}$	$V_{\text{meso}}, \text{cm}^3/\text{g}$	$V_{\text{micro}}, \text{cm}^3/\text{g}$
Al-NA	71	0.5532	0.5258	0.0274
RHA	78	0.2436	0.2161	0.0276
PHS/Al-NA	4	0.0269	0.0251	0.0018
PHS/RHA	2	0.0083	0.0075	0.0008

Journal Pre-proof

Table 2. XPS surface atomic concentrations (at.%)

Sample	Elements						
	C 1s	O 1s	N 1s	S 2p	Si 2p	Al 2p	Ca 2p
Al-NA	6	55	–	2	–	37	–
RHA	5	60	–	–	32	–	2
PHS/Al-NA	10	53	5	9	–	22	–
PHS/RHA	17	51	5	9	16	–	–

Journal Pre-proof

Declaration of interests

The authors declare that they have no known competing financial interests or personal relationships that could have appeared to influence the work reported in this paper.

The authors declare the following financial interests/personal relationships which may be considered as potential competing interests:

Journal Pre-proof

Author statement

The theoretical calculations on the electronic spectrum of the pure ionic liquid are conducted by Romyana Yankova.

A part of the activity behavior of the obtained catalytic systems is investigated by Anife Veli.

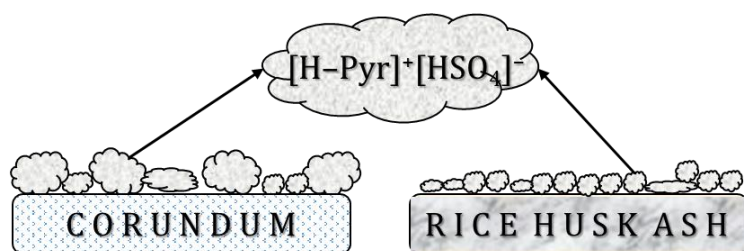
The FT-IR data were reordered by Radoslava Nikolova

The GC analysis for analysis of the acetic acid conversion was conducted by Zilya Mustafa.

The thermal analysis is conducted by Ivanka Stoycheva

The samples synthesis, catalysts activity, XPS measurements, experimental UV-vis, figures and tables representation, and manuscript writing is conducted by the corresponding author, Ivaylo Tankov

Graphical Abstract



Journal Pre-proof

Highlights

- Rice husk ash and corundum supported [H-Pyr]⁺[HSO₄]⁻ catalysts are investigated.
- More dispersed IL particles present on the RHA support surface than α -Al₂O₃.
- Al(Si)-O...H-N and Al(Si)-O-S bonds express the surface IL-support interactions.
- The [H-Pyr]⁺[HSO₄]⁻/RHA catalyst possesses a higher thermal stability.
- A superior catalytic behavior is observed in the case of the IL/RHA sample.

Journal Pre-proof